Analysis of Ground Motion at SPS and LEP - Implications for the LHC

Ralph J. Steinhagen[*], **Stefano Redaelli, Jörg Wenninger**

Abstract

This document presents an analysis of ground motion induced orbit drifts and presents two models describing the propagation and amplification of ground motion on the SPS, LEP, and LHC orbits qualitatively and quantitatively.

The analysis shows that the largest ground motion contribution to the orbit drift on the time scale ranging from seconds to a month is due to random ground motion and is barely influenced by correlated ground motion. An upper limit of the expected drifts at the LHC, SPS, and the TI8 and CNGS transfer lines due to ground motion only are given. The predictions are supported by beam measurements at LEP in 1999 and ground and beam motion based measurements performed in 2004 in the SPS and TI8.

---

[*]Doctoral Student at CERN and 3rd Institute of Physics, RWTH Aachen University

1 Introduction

The stability of the beams becomes an increasingly important parameter for safe and reliable machine operation of the LHC. The performance of the LHC Beam Cleaning System critically depends on orbit stability, with tolerances down to $\approx \frac{\sigma}{3}$ (σ = r.m.s. beam size) corresponding to $\approx 300\,\mu m$ at 450 GeV and $\approx 70\,\mu m$ at 7 TeV. There are numerous causes for orbit perturbations with excursions expected to largely exceed the required tolerances.

Orbit perturbation sources can be grouped into three classes:

1. Machine-inherent sources such as decay and snapback of the main dipoles' multipoles, changes of the final focus optics (squeeze), eddy currents on the vacuum chamber, ramp-induced effects, and flow of cooling liquids. The largest orbit perturbations can exceed 20 mm in the case of the beta squeeze.

2. Environmental sources such as ground motion, temperature, pressure changes, cultural noise, and other effects. These effects are propagated through the magnets (mostly the quadrupoles) and their girders to the beams.

3. Machine element failures particularly orbit correction dipole magnets (CODs) and beam separation elements

This analysis focuses on ground motion-induced orbit shifts on the time scale ranging from seconds to months. Long-term ground settlement effects such as those described and analysed for LEP [1] based on long-term alignment data are not within the scope of this analysis. We present two models to describe the propagation and amplification of correlated and uncorrelated ground motion on the SPS, LEP and LHC orbits.

2 The Accelerator Tunnels

The SPS and LHC/LEP tunnels have a circumference of about 6.9 km and 26.7 km respectively and an average depth of about 50 m and 100 m respectively. Both tunnels are embedded in the *Molasse*, a soft tertiary sandstone on top of a hard rock basin found in the region. The *Molasse* mainly consists of clay and limestone eroded from the surrounding Jura and the Alps and is covered by the *Moraine*, a loose and permeable more recent quaternary erosion from the Jura. An important feature of this geological formation is the different propagation speeds and refraction indices for ground waves in the Moraine and Molasse. Seismic faults and wells in the region of the accelerators are considered to be inactive and are neglected on the time scale ranging from a few hours to a month [2, 3].

3 Ground Motion Model

The main influence of ground motion on particle beams is through the displacements of quadrupoles and girders. A quadrupole misaligned by ϵ introduces a dipole kick δ proportional to its focusing strength k and length l, $\delta = kl \cdot \epsilon$. This dipole kick creates a perturbation $\Delta x(s)$ of the closed orbit that can be written as:

$$\Delta x(s) = \frac{\sqrt{\beta(s)\beta_j}}{2\sin(\pi Q)} \cdot \cos(\Delta\mu - \pi Q) \cdot \delta \tag{1}$$

Respectively, for a transfer line:

$$\Delta x(s) = \begin{cases} \sqrt{\beta(s)\beta_j} \cdot \sin(\Delta\mu) \cdot \delta & : & \Delta\mu > 0 \\ 0 & : & \Delta\mu \leq 0 \end{cases} \qquad (2)$$

The betatron oscillations depend on the values of the betatron-function at the location of the kick (β_j) and the observation point ($\beta(s)$); Q is the machine tune and $\Delta\mu$, the positive phase advance from the location of the dipole kick to the observation point. In general, the orbit is sampled at m beam position monitors (BPM). The displacement at monitor i due to n quadrupoles labelled by j is

$$\Delta x_i = \sum_{j=0}^{n} \frac{\sqrt{\beta_i\beta_j}}{2\sin(\pi Q)} \cdot \cos(\Delta\mu_{ij} - \pi Q) \cdot k_j l_j \cdot \epsilon_j \qquad (3)$$

respectively for transfer lines:

$$\Delta x_i = \sum_{j=0}^{n} \begin{cases} \sqrt{\beta_i\beta_j} \cdot \sin(\Delta\mu) \cdot k_j l_j \cdot \epsilon_j & : & \Delta\mu > 0 \\ 0 & : & \Delta\mu \leq 0 \end{cases} \qquad (4)$$

Both equations can be written in form

$$\Delta x_i = \sum_{j=0}^{n} R_{ij} \cdot \epsilon_j \qquad (5)$$

where R_{ij} is the element of the $m \times n$ orbit response matrix and depends on the machine optics. In order to be less dependent on the value of the beta-function at the specific BPM and to give results in terms of beam size, it is useful to normalise Equation 5 by $\sqrt{\beta_i}$

$$\Delta x_i/\sqrt{\beta_i} = \sum_{j=0}^{n} (R_{ij}/\sqrt{\beta_i}) \cdot \epsilon_j \qquad (6)$$

$$\Delta\tilde{x}_i = \sum_{j=0}^{n} \tilde{R}_{ij} \cdot \epsilon_j \qquad (7)$$

The average effect of misaligned quadrupoles (average quadrupole movement $\bar{\epsilon}$) onto the normalised ($\tilde{\sigma}$) and un-normalised orbit r.m.s. σ can be approximated by factors κ and $\tilde{\kappa}$ respectively:

$$\sigma = \sqrt{\frac{1}{m}\sum_{i=0}^{m}\Delta x_i^2} = \kappa \cdot \bar{\epsilon}$$

$$\tilde{\sigma} = \sqrt{\frac{1}{m}\sum_{i=0}^{m}\Delta x_i^2/\beta_i} = \tilde{\kappa} \cdot \bar{\epsilon} \qquad (8)$$

More generally, the cumulative effect of the ground movement on the orbit strongly depends on the frequency and spatial correlation of the movements. The relation between the power spectrum distribution (PSD) or r.m.s. movement of the ground motion (S_{gm}) and the orbit (S_{orbit}), assuming a rigid girder response, can be approximated using the factor $\kappa(f)$ to:

3

$$S_{orbit}(f) = \kappa^2(f) \cdot S_{gm}(f) \tag{9}$$

respectively,

$$\tilde{S}_{orbit}(f) = \tilde{\kappa}^2(f) \cdot S_{gm}(f) \tag{10}$$

To simplify the analysis, the movement can be decomposed into random (fully un-correlated) and coherent (fully correlated) ground motion.

3.1 Random Ground Motion

For the application in the SPS and LEP/LHC model, one can assume that the accelerator tunnels are entirely embedded in a homogeneous ground. While this is certainly true for the SPS, the assumption holds for the LEP/LHC tunnel as well, since only about $3\,\mathrm{km}$ of the $27\,\mathrm{km}$ circumference is located in hard rock regions of the Jura mountains.

For random misalignment, the optical amplification factor κ of Equation 9 is independent of the exciting frequency. For a regular FODO lattice with N cells, κ can analytically be approximated to (see Annex):

$$\kappa = \frac{kl\beta_{eff}}{4\sin(\pi Q)} \cdot \sqrt{N} \tag{11}$$

Here kl is the average integrated quadrupole strength, Q the tune and β_{eff} the effective beta function, $\beta_{eff} = \sqrt{\beta_{QF}^2 + \beta_{QD}^2}$, with $\beta_{QF(D)}$ the betatron function at the horizontal (de-) focusing quadrupoles. This approximation is useful for qualitative purposes and regular FODO lattices. However, it underestimates non-regular lattices with insertions having large quadrupole strengths and large values of beta functions. The choice of fractional tune critically influences the size of the optical amplification due to the factor $\sin(\pi Q)$ in the denominator of Equation 11. For comparison, the analytical amplification factors of the SPS and LHC arc FODO lattice (Equation 11) are given in the following table.

	horizontal		vertical	
	κ	$\tilde{\kappa}$	κ	$\tilde{\kappa}$
SPS	31	3.0	23	2.2
LEP	36	3.1	48.2	2.4
LHC	26	1.9	20	1.5

Table 1: Approximate propagation factors for random motion as given by Equation 11 for the SPS, LEP, and LHC arc FODO cells.

To take all details of the optics into account (like final focus, varying phase advances, etc.), κ is evaluated numerically using Equations 3, 4 and 9. For each sample, all quadrupoles are misaligned. The computed ratio between quadrupole shift and resulting orbit r.m.s. is used to evaluate the individual amplification. The average and r.m.s spread of κ are evaluated from 10^5 samples for a given optics and plane. Since ground motion affects all elements, a corrective BPM shift was applied. In case a BPM is installed next to a quadrupole, it is assumed that the BPM is rigidly connected to the corresponding quadrupole. Otherwise, the BPM is shifted

independently. This approximation is valid for LHC and LEP as nearly all BPMs are directly mounted on the quadrupoles. At the SPS, the BPMs are not mounted on the same girder than the quadrupoles, but are very close ($\approx 1\,\mathrm{m}$) to the quadrupoles, such that the 'rigid connection' approximation may still be valid. The simulations are performed for the SPS (with LHC beam tunes, $Q_H = 26.13$ and $Q_V = 26.18$), LEP (1999 collision optics, $Q_H = 98.28$ and $Q_V = 92.20$) and LHC (version 6.5, injection and collision optics, $Q_H = 64.28$ and $Q_V = 59.31$). The simulations for the TI8 and CNGS transfer lines are performed similarly, with the exception of the modified beam transfer function. These κ values correspond to the orbit drift at the last TI8 TED (mobile dump) and the CNGS target respectively. Table 2 summarises the results.

	horizontal		vertical	
	κ	$\tilde{\kappa}$	κ	$\tilde{\kappa}$
SPS	40.6 ± 19.3	3.1 ± 1.4	30.1 ± 13.3	4.1 ± 2.0
LEP coll	34.3 ± 13.7	5.0 ± 2.0	119.5 ± 65.7	11.2 ± 6.1
LEP coll*	34.3 ± 13.7	5.0 ± 2.0	58.6 ± 25.9	5.6 ± 2.4
LHC inj	30.5 ± 11.5	3.2 ± 0.8	29.6 ± 9.0	3.0 ± 0.7
LHC coll	63.3 ± 32.5	5.2 ± 2.0	62.1 ± 25.5	4.9 ± 1.9
TI8 TED	19.5 ± 14.6	1.8 ± 1.3	10.6 ± 8.0	1.6 ± 1.2
CNGS target	4.2 ± 3.2	1.3 ± 1.0	4.9 ± 3.6	1.1 ± 0.8

Table 2: Simulated orbit amplification factor κ for randomly misaligned quadrupoles. The LHC collision optics (version 6.5) includes the final focus to $\beta^* = 0.55\,\mathrm{m}$ in IR1 (ATLAS) and IR5 (CMS). The LEP '*' values do not include the systematic shifts due to the low-beta quadrupoles (QS0) around the four interaction regions.

The spread of κ given in Table 2 is an intrinsical uncertainty due to the sensitivity of the response to the exact "seed" of the movement. The actual individual amplification is expected to be within these limits with a probability of about 68%. The amplification analysis shows that LEP was more sensitive to vertical random ground motion than the LHC. The large difference of the κ factors between the LHC and LEP collision optics is due to the very strong vertical focusing around the interaction region in LEP. In LEP, the insertion quadrupoles contribute to about 50% of the total κ value. Removing these quadrupoles ("QS0") yields comparable numbers for LEP and LHC.

One can use a BROWNIAN process to model time dependence of the random motion of each individual quadrupole as well as to describe the physical properties of the measured data. We ignore, while discussing the propagation of random ground motion only, any coupling between planes and spatial correlation. In this simple model, each quadrupole movement is described by STOKE's differential equation for a viscous medium. The equation describes the dependence of the position x of a damped (α being the damping factor) mass m under influence of an external randomly varying force $F(t)$:

$$m\ddot{x} + \alpha\dot{x} = F(t) \tag{12}$$

A more complete and more complex model would include spring-like retracting force ($+kx$) acting on very large excursions, constant and coupling forces. Though an analytical solution of

equation 12 and a direct prediction of the random movement, is not possible, one can derive the following important statistical properties of this type of motion, as shown in the Annex:

1. For long-time scales, the mean random movement $\mu = \langle x \rangle$ vanishes:

$$\lim_{t \to \infty} \mu = 0 \qquad (13)$$

2. For large time scales the root-mean-square $\sigma = \sqrt{\langle x \rangle^2 - \mu^2}$ of Brownian motion increases proportionally to the square root of time as derived in the Appendix (A being the diffusion constant):

$$\lim_{t \to \infty} \sigma_{rms} = A \cdot \sqrt{t} \qquad (14)$$

3. The power spectrum (density) shows a typical 'brown'-noise $\frac{1}{f^2}$ dependence on the frequency.

3.2 Coherent Ground Motion

There is a broad frequency spectrum of coherent ground motion sources that affect the orbits:

1. Natural sources such as ground settlement, tectonic motion, tides, earthquakes, microseismic noise, climate changes, tunnel temperature and atmospheric pressure changes, change of water levels (lake or ground), ...

2. Cultural noise, such as noise due to human activity on the surface, such as railroad traffic, trucks, cars, civil construction, etc.

3. In situ tunnel equipment: cooling water and cryogenic coolant flow, ventilation, motors, mechanical vibrations of magnets due to time-varying fields...

Only coherent ground waves with source locations outside the tunnel perimeter are considered for the propagation model. These can, in the far field, be described by plane waves. Ground settlement, potential fault activity and tunnel equipment specific vibrations are neglected.

Rayleigh waves are the most important ground waves that dominate the coherent background. Found only near the surface, they are created through interference of longitudinal "pressure" and transverse-"shear" waves (further referred to as P- and S-waves) from deeper regions while travelling to the surface. Rayleigh waves have longitudinal and vertical particle oscillation with respect to the propagation direction, and the particles describe retrograde ellipses as shown in Figure 1.

P-, S- and Rayleigh wave propagation velocities differ, fulfilling the relation $c_p > c_s > c_{Rayleigh}$. To first order, the density of the ground increases with depth. Since the propagation velocity of sound is a function of density, Rayleigh waves have a dispersion relation depending on depth and consequently lose their coherence with depth (dissipation) as well. The accelerator depth is almost constant and hence the dispersive effect is ignored in this analysis. The analytical solution for P-, S- and surface Rayleigh waves for a point source (wavelength λ) show that the damping D at a distance r from a reference position ($r_0 > \lambda$) can be decomposed into three parts, geometric, dissipative (Q_d, site specific quality factor ranging from 10-25 for near surface to several hundreds for hard rock) and depth dependent part (h: depth) as shown in the following equation:
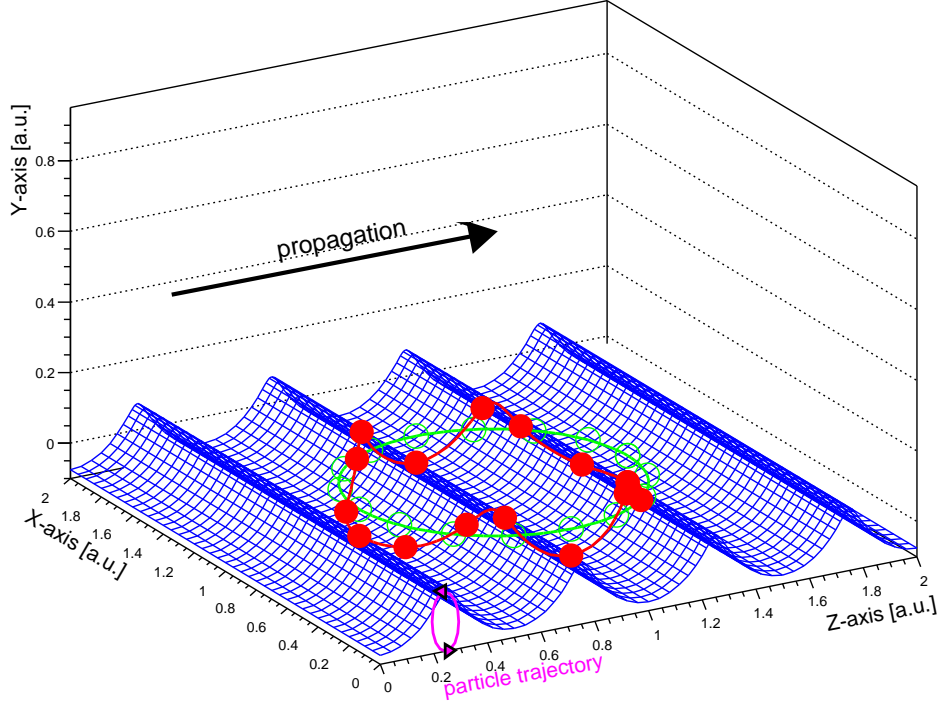
Figure 1: Example of an accelerator that is unperturbed (green) or perturbed by a Rayleigh wave (red). The wave consists of transverse and longitudinal oscillations. The particles describe a retrograde ellipse with respect to the propagation direction.

$$D_{\mathrm{R}} = \sqrt{\frac{r_0}{r}} \cdot e^{-\frac{\pi(r-r_0)}{Q_d\lambda}} \cdot e^{-\frac{h}{\lambda}} \tag{15}$$

$$D_{\mathrm{P/S}} = \frac{r_0}{r} \cdot e^{-\frac{\pi(r-r_0)}{Q_d\lambda}} \tag{16}$$

Though their wavefront arrives later, Rayleigh waves carry most of the energy over long distances and prevail over P- and S-waves because of the reduced geometric damping (Rayleigh waves $\sim r^{-0.5}$ vs. $\sim r^{-1}$ for P- and S-waves). The depth dependent damping of Rayleigh waves favours deeper underground tunnels as quiet locations. For example, assuming a wavelength of $\lambda = 50\,\mathrm{m}$, an increase of the tunnel depth from $50\,\mathrm{m}$ to $100\,\mathrm{m}$ has about twice the damping effect than doubling the distance to the source. In addition, ground waves die out faster as the wavelength decreases. Consequently, the coherence (or correlation) length, which is the maximum distance of two points oscillating coherently decreases rapidly with frequency and distance, as shown by measurements in the LEP and TT2 tunnels [10]. These measurements are reproduced in the Appendix, since this document is difficult to obtain.

The geological configuration around Geneva has an additional effect on the propagation of coherent waves. Molasse and Moraine have different propagation velocities that correspond to different refraction indices for these type of waves. Similar to light optics, coherent waves created on the surface due to, for example, human-induced 'cultural noise', will be partially reflected, partially transmitted and refracted at the boundary layer between Moraine and Molasse causing an additional reduction of those amplitudes inside the tunnel. Under certain conditions

of wavelength and incidence angle with respect to the boundary layer, these waves may even be totally reflected without penetrating the Molasse layer. As will be shown later, the largest contribution of coherent ground motion in the LHC tunnel is less due to the cultural activity on the surface, but rather due to long range effects like the 'ocean hum'.

The amplification factor $\kappa(f)$ of Equation 9 was evaluated for coherent waves from a simulation of the accelerator motion. Although there is no simple approximation to describe the waves motion in the near field, one can, for the far field and constant depth, approximate Rayleigh waves by a superimposition of plane P- and S-waves with the same propagation velocity for both planes as shown in Figure 2.
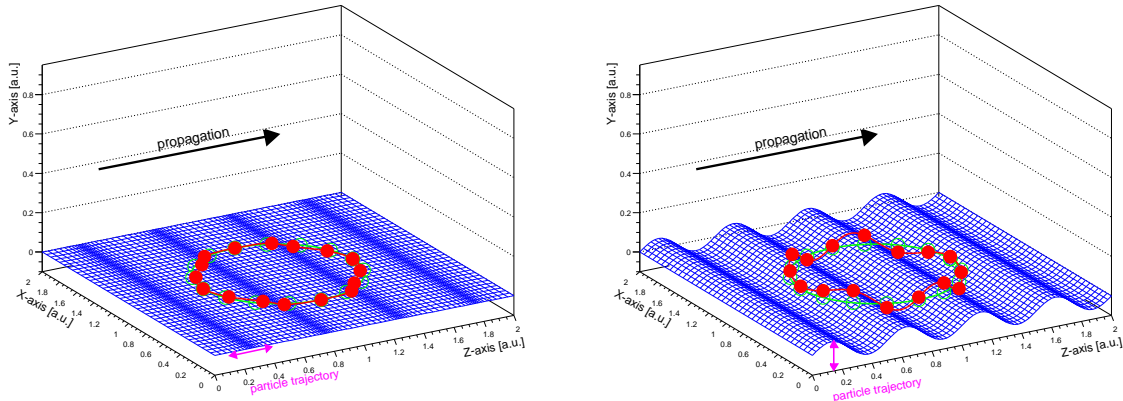
Figure 2: Perturbed (red) and unperturbed accelerator (green). Left: Example of a horizontal P-wave oscillation, when the particles oscillate longitudinally with respect to the wave propagation. Right: S-wave oscillation, the particles oscillate transversely with respect to the wave propagation.

This calculation extends earlier results described in [14] that were done for the vertical plane (S-waves) only using an early LHC optics and one main wave incident direction.

The proposed propagation model does not include the dissipative and dispersive nature of the ground that may cause a reduction of the coherence after some distance. Further, it is assumed that the drifts are sufficiently slow so that the orbit moves adiabatically.

For the simulation, the quadrupoles are misaligned according to the wave equations and the machine's geodesy data. For the BPMs, the same corrective shifts are applied as for the analysis of random ground motion. The beam response $\kappa(f)$ is defined by the ratio between orbit r.m.s. and ground wave amplitude. The response factors are averaged over different wave phases. The error band in the figures corresponds to the r.m.s. spread over the possible wave phases range. The wave incidence was varied as a second parameter. The 'zero-degree' angle corresponds to a wave propagation direction parallel to the axis going through IP5 (CMS) and IP1 (ATLAS).

The results are computed and given as a function of ground motion wavelengths. However, in order to relate the wavelengths to ground motion frequencies, an approximated Rayleigh wave propagation velocity of 2000 m/s, which is typical for the *Molasse* at the LHC depth is used. The actual propagation velocity may differ. The results for the SPS are shown in Figures 3 and 4 and the results for the LHC injection and collision optics are shown in Figures 5 and 6. The error bands correspond to r.m.s. spread. One can separate the spectra into three regions:

1. Low frequency region: the amplification κ vanishes since the wavelength exceeds the

accelerator diameter and the whole machine is lifted (S-wave) or shifted (P-wave) coherently.

2. Betatron resonance region: Resonant amplification occurs once the wavelength λ (frequency f) drops below the first harmonic of the betatron-wavelength λ_{beta} and the frequency f_{beta} respectively,

$$
\begin{aligned}
\lambda_{beta} &\approx \frac{C}{Q}, \\
f_{beta} &\approx \frac{v}{\lambda_{beta}},
\end{aligned}
\tag{17}
$$

C is the accelerator circumference and v the propagation velocity of the ground wave. For the LHC, the betatron-wave length is about 415 m and 450 m for the horizontal and vertical plane. In the SPS, the betatron-wavelength is about 264 m for both planes.

3. Moire-like pattern regime: Once the wavelength exceeds the minimum distance between quadrupoles l_{min}, the regular harmonic resonances become less important. The amplification is determined by the absolute phase relations between the wave front and individual element location and the local optics. For example, in the case of LHC collision optics, the effect of the insertion quadrupoles becomes increasingly visible once the ground wavelength is about the same distance as between the triplets around the experimental insertion regions. Further, it is visible that the averaged response functions for very high frequency are about the same as the amplification factor for random ground motion as given in Table 2.

Apart from the 8- and 6-fold symmetry, due to the long straight sections of the LHC and SPS, respectively, the LHC injection and SPS amplification spectra do not not show any significant angle dependence. The LHC collision optics has a small dependence on the wave propagation direction as seen in Figure 7. The vertical amplification factor is larger for S-wave propagation along the IP3-IP6 axis above about 30 Hz, corresponding to the resonant mode of the inner triplets in IP1 and IP5. The horizontal amplification factor dependence on angles is rather small but is visible above 30 Hz. The dependence on the propagation direction is mainly visible above l_{min}, where its effect is basically negligible, as the wave is likely to completely lose either its coherence or its energy over a fraction of the accelerator dimension. This is due to the strong dissipative effect of the ground for high frequencies (Equation 15), and confirmed by coherence length measurement performed in the TT2 tunnel [10] (see Appendix for reprint of figures).
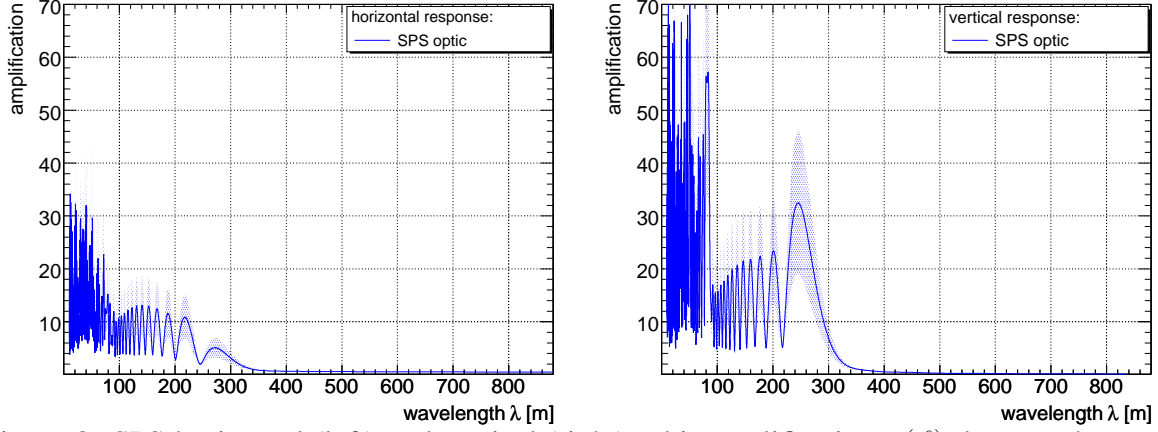
9

Figure 3: SPS horizontal (left) and vertical (right) orbit amplification $\kappa(f)$ due to coherent P- and S-wave oscillations. The amplification is shown as a function of wavelength. The first resonance once the wavelength drops below the betatron-wavelength of about 264 m is visible.
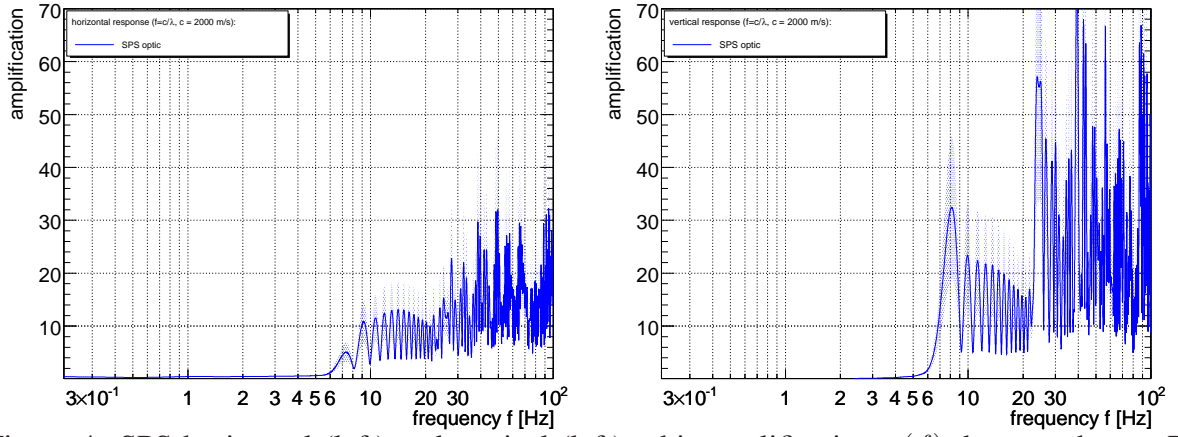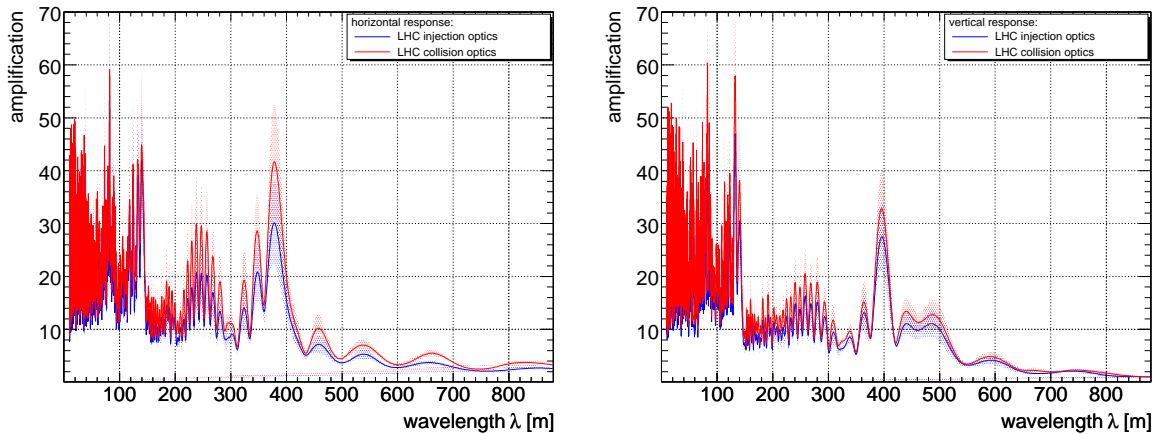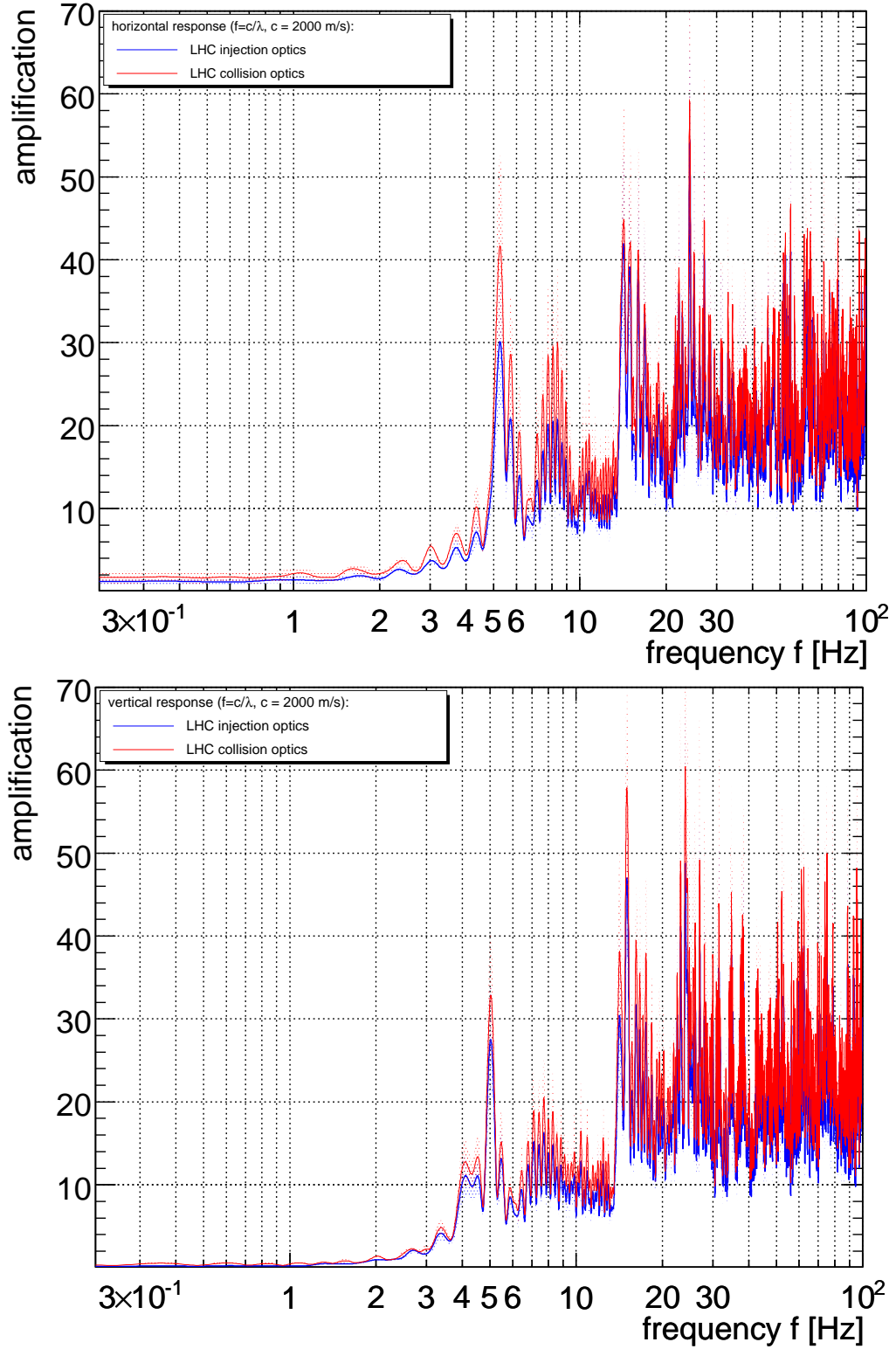

Figure 4: SPS horizontal (left) and vertical (left) orbit amplification $\kappa(f)$ due to coherent P- and S-wave oscillations. The amplification is shown as a function of wavelength (right) and frequency (left) assuming a ground wave propagation velocity in the *Molasse* of $c = 2000\,\mathrm{m/s}$.

Figure 5: LHC horizontal (left) and vertical (right) orbit amplification $\kappa(f)$ due to coherent P- and S- wave oscillations. The first resonance once the wavelength drops below the betatron-wavelength of about 415 m (horizontal) and 450 m (vertical) is visible.

Figure 6: LHC horizontal (top) and vertical (bottom) orbit amplification $\kappa(f)$ due to coherent P- and S- wave oscillations. The amplification is shown as a function frequency assuming a ground wave propagation velocity in the *Molasse* of $c = 2000\,\mathrm{m/s}$.
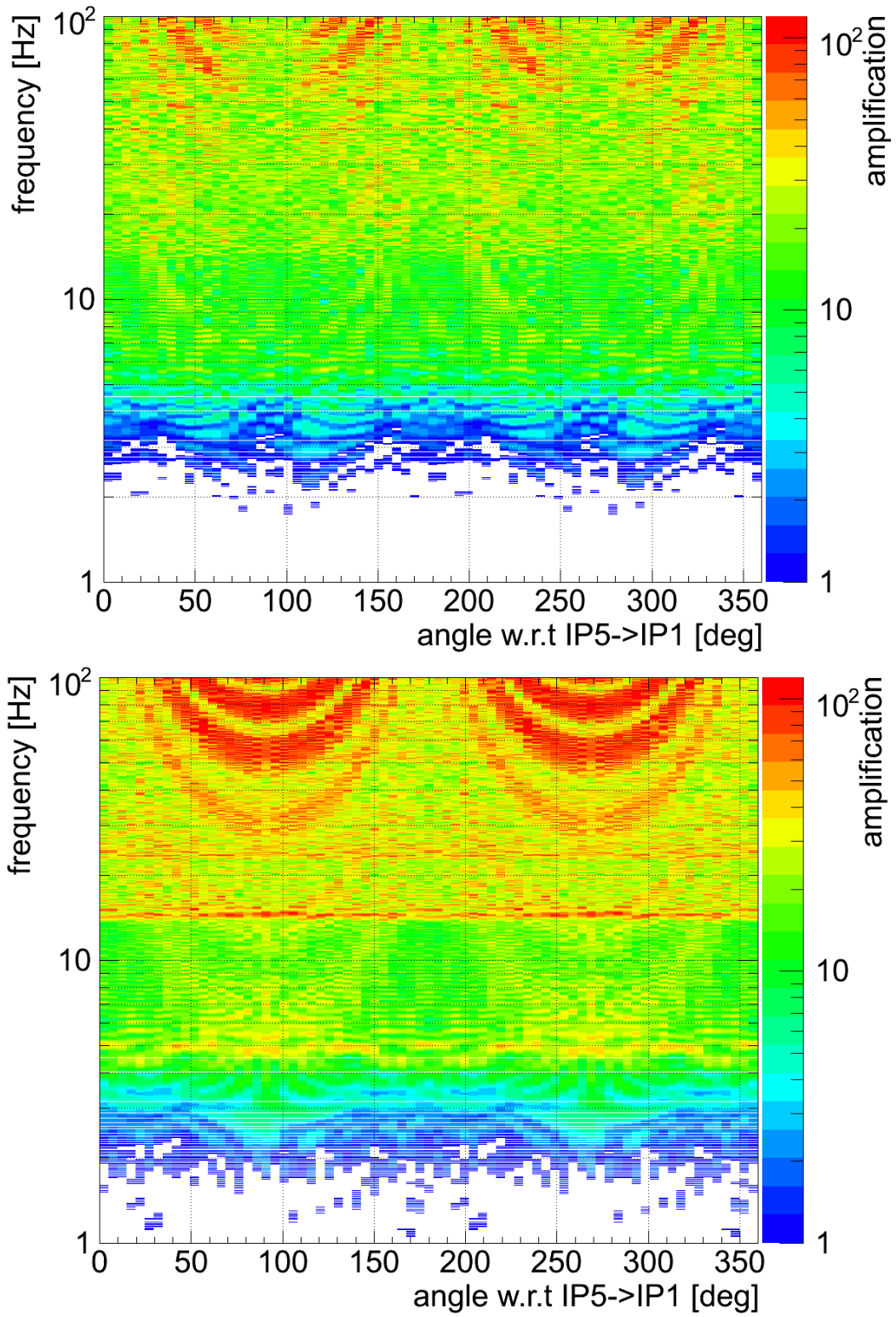
11

Figure 7: LHC amplification factor dependence on the propagation direction for the horizontal (top) and vertical plane (bottom). The 'zero-degree' angle corresponds to a wave propagation direction parallel to the axis going through IP5 (CMS) and IP1 (ATLAS).

12

4   Comparison with Experimental Data

4.1   Seismic measurements

In 2004, long-term seismic SPS tunnel vibrations and SPS beam drifts were studied. The seismic measurements were performed in the SPS tunnel with a *Guralp CMG-40T* type geophone. The device measures the transverse, longitudinal, and vertical velocity of a damped test mass at a rate of 200 Hz. The sensitivity decreases for very high and very low frequencies, resulting in an underestimation of amplitudes. After calibration, the device is sufficiently linear inside the frequency band from 0.03 to 50 Hz. The probe was positioned such that the reference system corresponds to the accelerator system where 'longitudinal' refers to the axis along the tunnel, the 'tranverse' axis pointing outwards, and the 'vertical' axis pointing upwards.

The data was taken between Tuesday, 9th March 2004 and Monday, 14th March 2004 on the ground at the SPS quadrupole QF.522. During the data collection period, installation work was performed in the vicinity (≈ 100 m). Data was acquired every half an hour for a duration of 6 minutes. The sensor sensitivity vanishes for periods larger than 30 s. In order that the Fourier transform is not the limiting factor of the resolution and sensitivity, the analysis window was chosen to be 60 s long. The individual spectra of one acquisition are averaged to reduce noise. We use the Fast Fourier algorithm described and defined in [11]. The velocity spectra ($P_v(f)$) are converted to amplitude spectra ($P_x(f)$) using the following relation:

$$P_x(f) = \frac{1}{(2\pi f)^2} P_v(f) \tag{18}$$

The general Fourier transform only specifies that the forward-backward transform of a signal has to yield the same signal but does not explicitly specify the normalisation of the spectra. Hence, there are numerous different FFT spectra definitions. We use the following spectra normalisation in the presented figures: a coherent sinusoidal signal with a constant amplitude A corresponds to an amplitude A^2 in the power spectra and to an amplitude $A^2/\mathrm{d}f$ in the power density spectra ($1/\mathrm{d}f$ being the length of the Fourier window). Power spectra (squared Fourier spectra) are better suited for coherent signals, whereas power spectrum density representation is more appropriate when dealing with random signals. For reference, data is given in both forms. For purely random signals, the long-term drift due to frequencies $\geq f$ is obtained from the discrete *integrated r.m.s.* definition

$$I(f) = \sqrt{\sum_{f}^{f_{max}} \mathrm{PSD}(f)\Delta f} \tag{19}$$

with $\mathrm{PSD}(f) = P_x(f)/\Delta f$ being the power spectra density and Δf the frequency bin width. This definition is not valid for a superposition of coherent signals. It is important to note that geophones measure the combined effect of random and coherent ground motion. Direct propagation and conclusion from the measured ground motion spectrum to the beam, without knowing the apportionment between the random (correlated) and coherent (un-correlated) part of the spectrum, is generally not possible.

In order to identify the type, coherence, and potential period of a signal, the auto-correlation

13

function can be used that is defined as:

$$A(t) = \int_{-\infty}^{+\infty} x\,(\tau) \cdot x\,(t - \tau)\,\mathrm{d}\tau \tag{20}$$

Figure 8 shows the averaged spectra for the longitudinal, horizontal, and vertical planes acquired during quiet periods (weekend). The $\frac{1}{f^2}$ dependence that is typical for random motion and drifts and the peak around 0.1 Hz due to ocean hum is visible. Longitudinal, horizontal and vertical
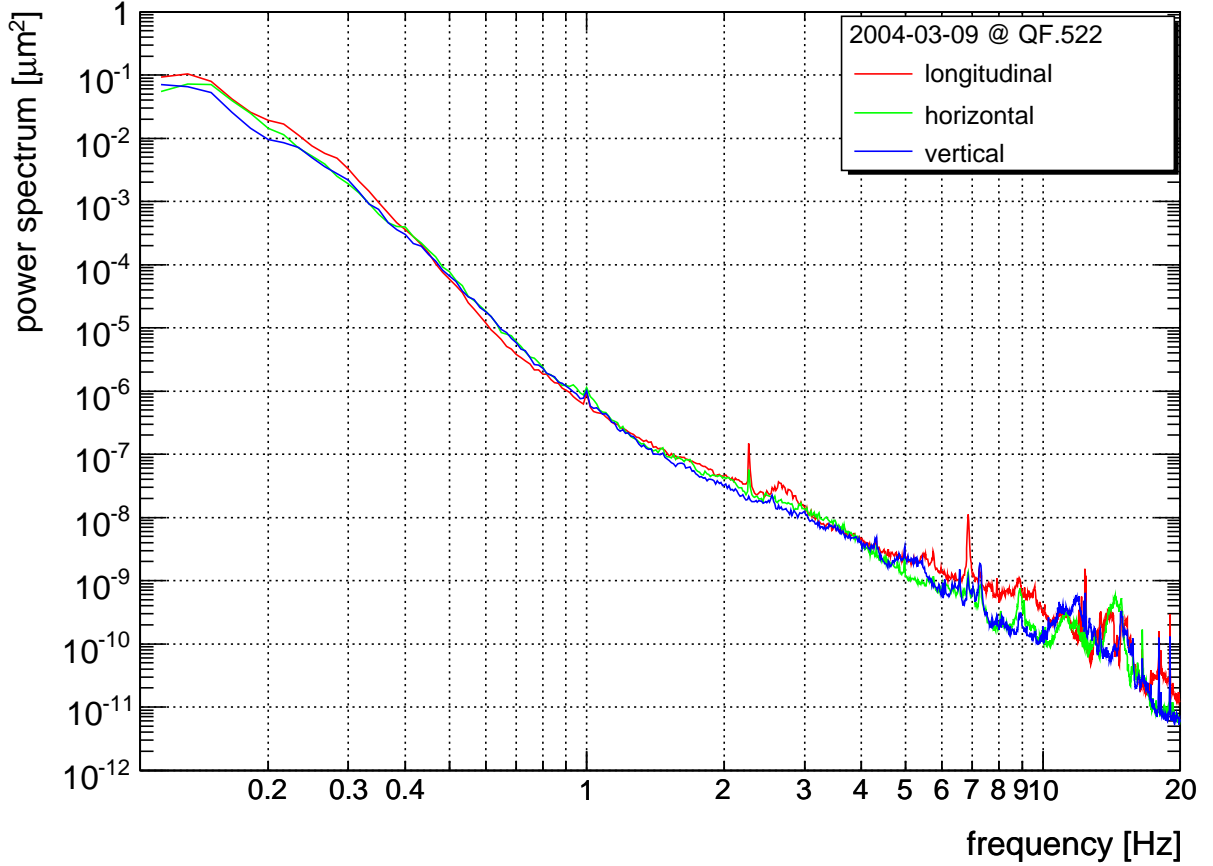

Figure 8: Averaged ground motion power spectra in the SPS taken at quadrupole QF.522. The spectra for the different planes are to first order identical, but show slightly stronger amplitudes for the longitudinal and horizontal planes, compatible with the elliptical motion of Rayleigh ground waves that predict the asymmetry.

power spectra have similar magnitudes. This is compatible with Rayleigh waves. It is visible that the contribution due to cultural noise vanishes during lunch times, indicating that the noise is largely due to civil construction activity in the tunnel and less due to the surface activities.

A comparison of typical vertical SPS and LEP/LHC ground motion spectra is shown in Figure 9. Both tunnels are very quiet and are barely influenced by cultural noise. The spectra are essentially the same. Since both accelerators are embedded in the same ground, it is possible to use SPS orbit data to predict orbit drifts at the LHC, provided the respective factors arising from the beam optics are understood.
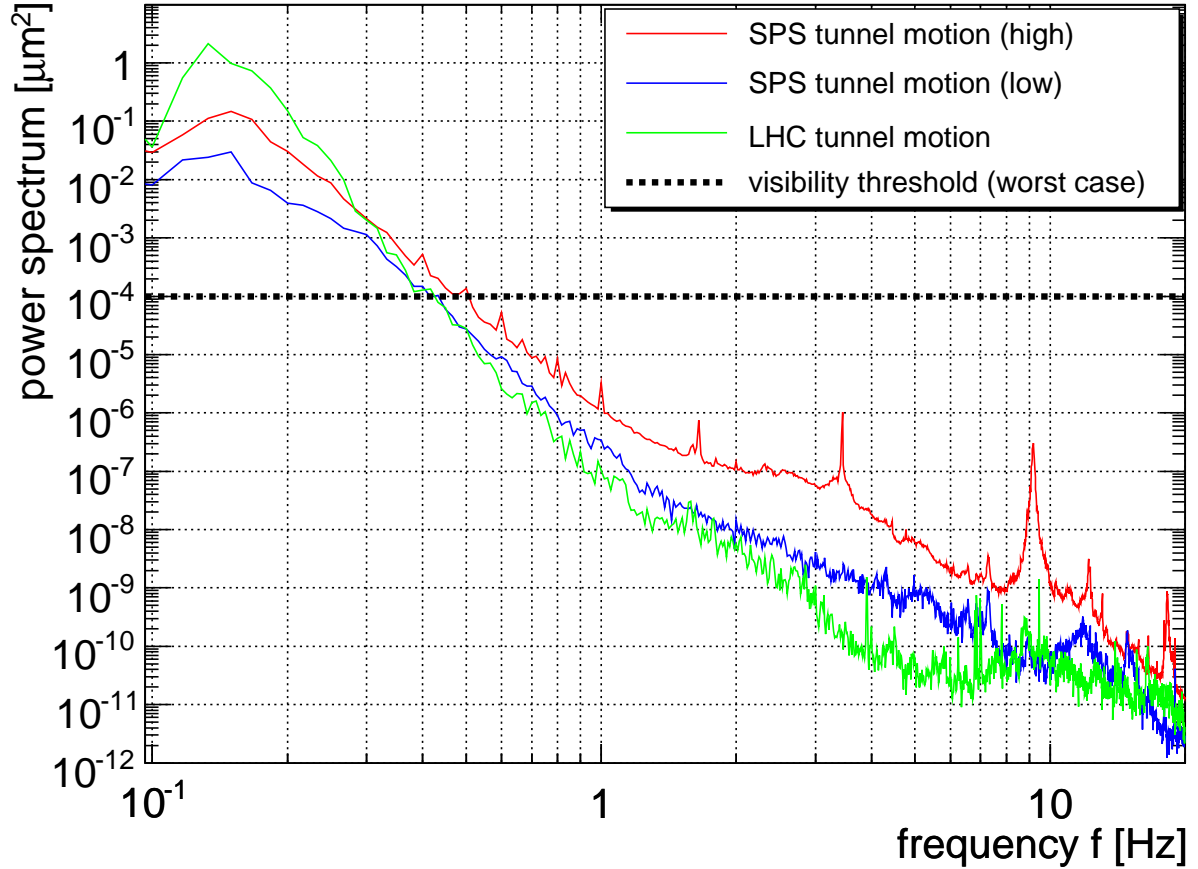
Figure 9: Averaged ground motion power spectra in the SPS and LHC tunnel. The 'high' SPS spectrum was recorded during a period of ongoing installation work. The visibility threshold corresponds to the ground-motion level having a 1 μm effect on the beam, assuming a worst-case constant propagation factor $\kappa = 100$.

For the LHC, random ground motion dominates over coherent ground motion. Though the latter may have a stronger amplification of up to a factor of $\kappa(f) \approx 60$ for frequencies above 3 Hz, they contribute less because the power spectra decreases rapidly above this frequency. From Figure 9, and assuming $\kappa \approx 100$, it is clear that ground motion above 1 Hz should not pose a problem at the LHC, whether the movement is coherent or not, assuming that the girder response does not show significant resonances.

Typical power spectra (densities) are shown in Figure 10, and the corresponding integrated r.m.s. are shown in Figure 11. The auto-correlation spectra as a function of acquisition time are shown in Figure 13. A repetitive pattern with a period of about 7 s is visible. Cultural noise, such as installation work in the tunnel, manifests itself mainly in the 1 to 10 Hz frequency band, as visible in Figure 14. The integrated r.m.s oscillation above 1 Hz is modulated between about 200 and 800 nm, see Figure 12.
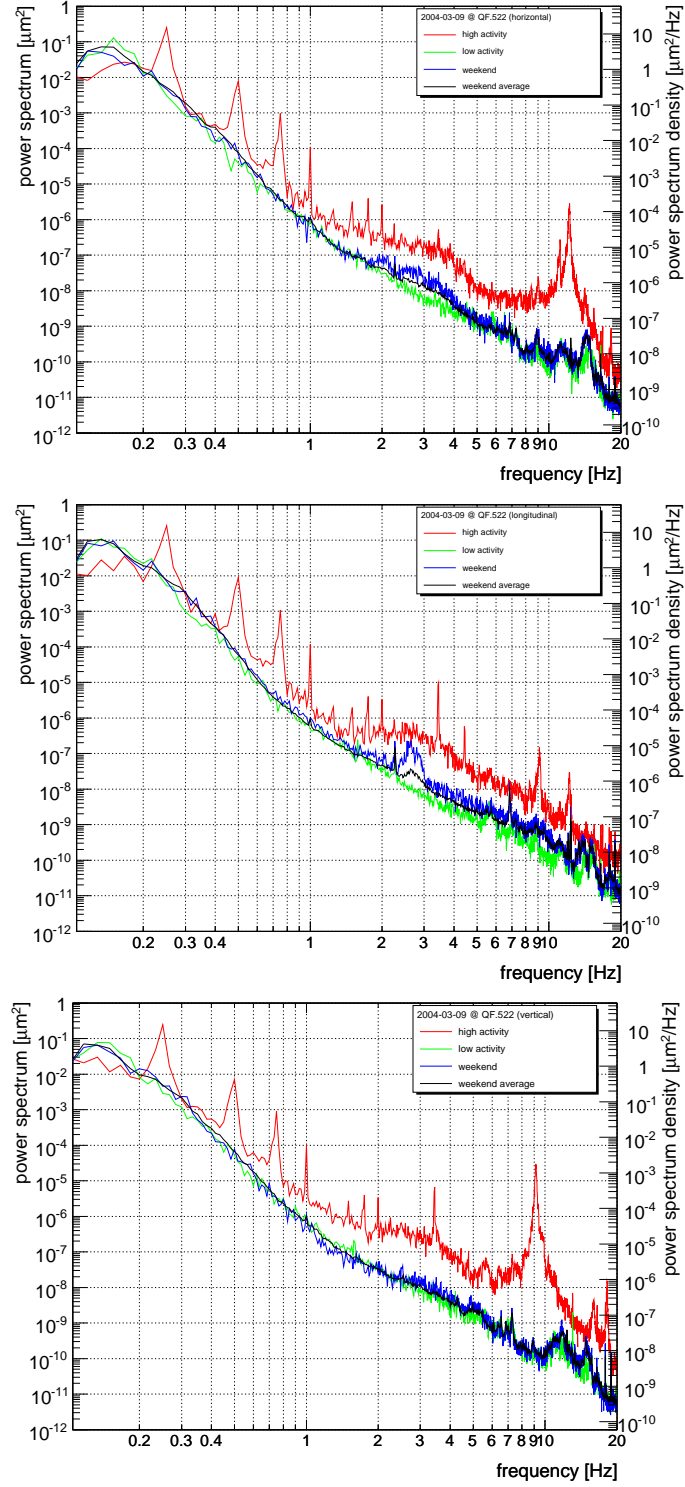
Figure 10: Horizontal (top), longitudinal (middle) and vertical (bottom) ground motion spectrum (densities) measured in the SPS tunnel. The 'high activity' spectra correspond to measurements performed during periods of equipment installation in the vicinity of the geophone ($\approx 100\,\mathrm{m}$).
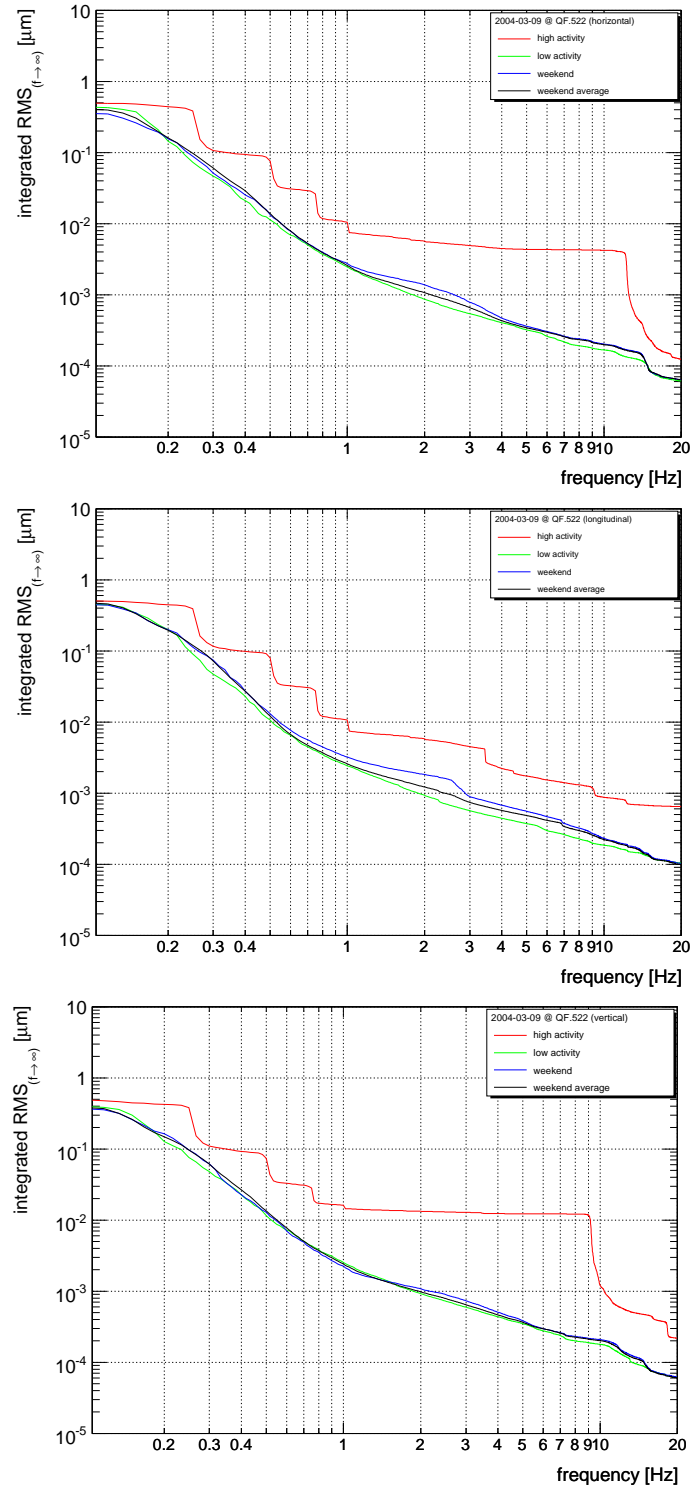
Figure 11: Horizontal (top), longitudinal (middle) and vertical (bottom) integrated ground motion spectrum. In normal conditions, the integrated r.m.s. is less than about 2 nm for frequencies above 1 Hz.
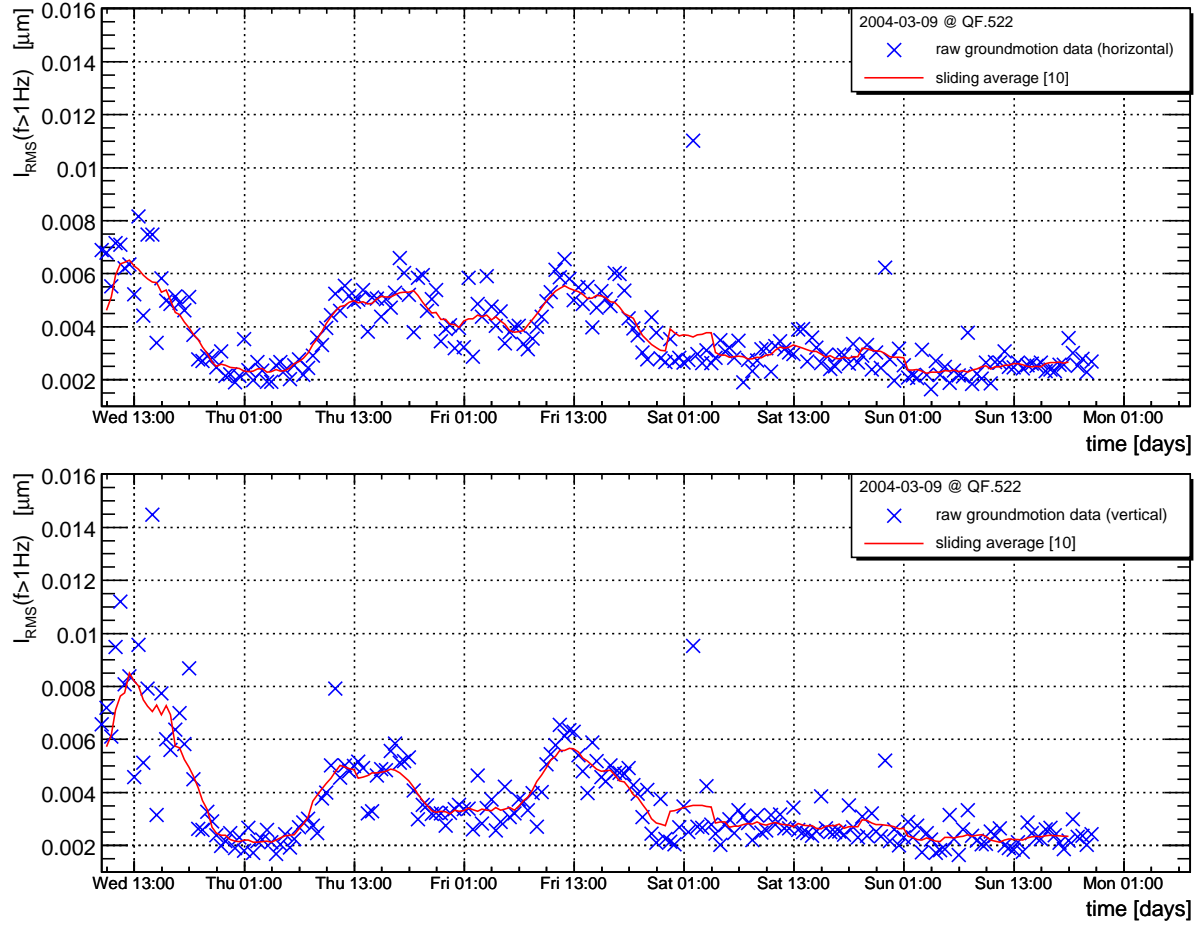
Figure 12: Horizontal (top) and vertical (bottom) integrated r.m.s. for frequencies above 1 Hz. The day-night cycle that is visible during the week is due to installation work in the tunnel. The amplitude of the cultural noise varies between about 200 and 800 nm.
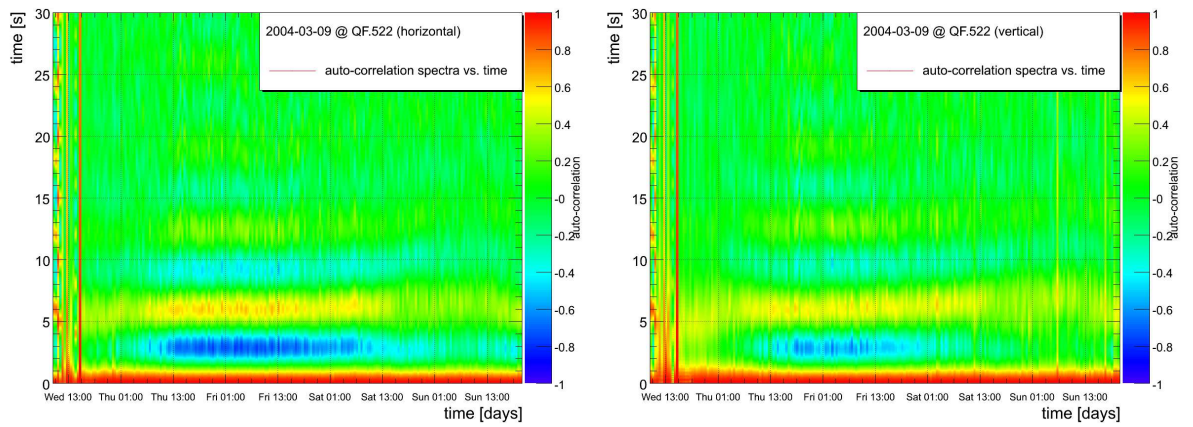

Figure 13: Horizontal (left) and vertical (right) auto-correlation spectrum. The coherent signal around with a period of about 7 s corresponds to the ocean hum. The decrease of amplitude for long time periods is an artefact of the autocorrelation function due to the finite acquisition window.
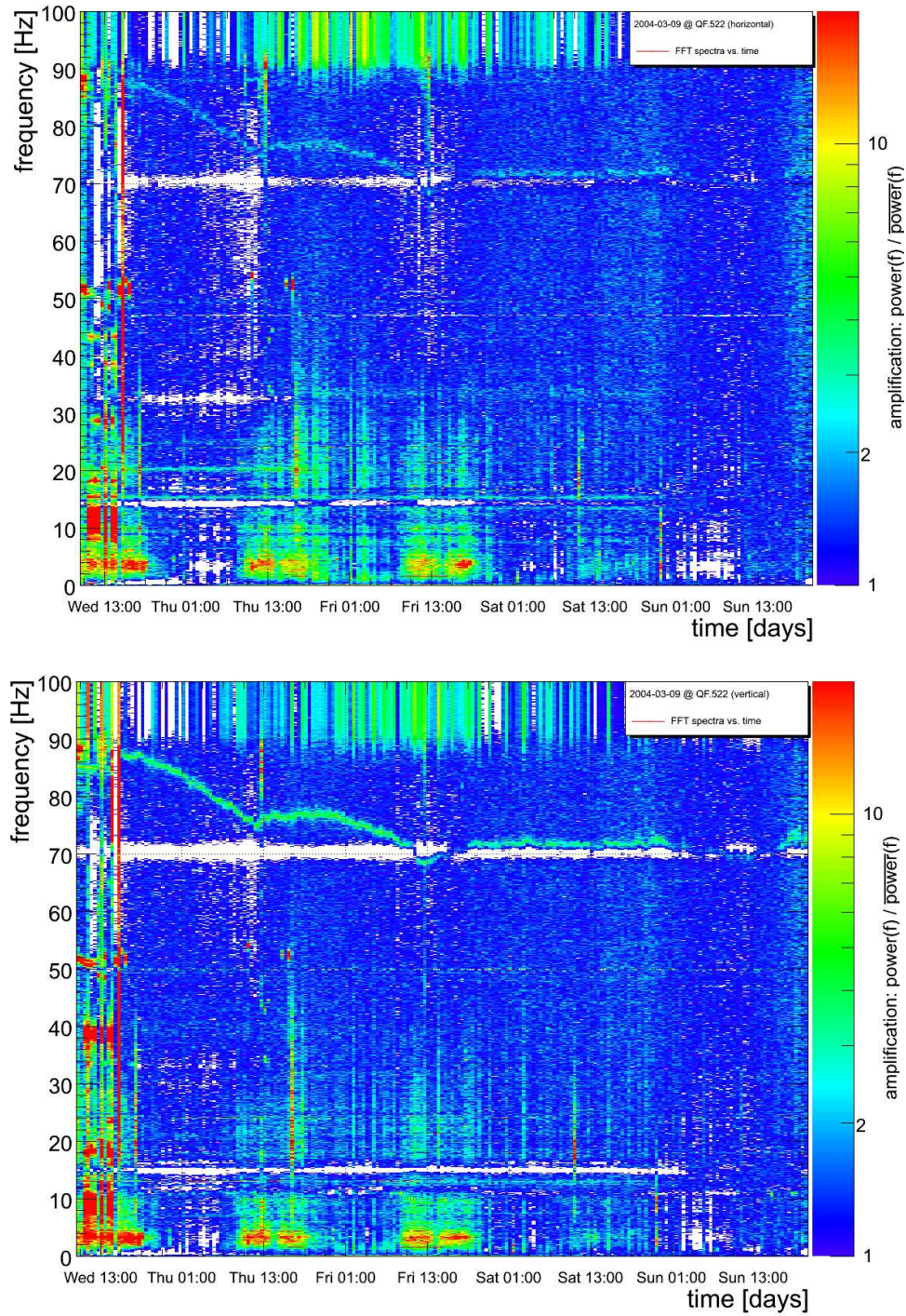
Figure 14: Horizontal (top) and vertical (bottom) ground motion spectrum as a function of acquisition time. The spectra are normalised to the averaged low activity (weekend) spectra. Some cultural noise is visible in a frequency band between 1 and 10 Hz. The day-night cycles during the work week and the reduced noise level during the weekend are visible. The regular gaps during days with activity in the tunnel correspond to the lunch break.

4.2 SPS Orbit Measurements

In 2004 long-term orbit stability measurements were performed with a 270 GeV coasting beam in the SPS. Figure 15 shows an example of the vertical beam motion power spectra of a 270 GeV and 26 GeV coasting beam in the SPS that was sampled at a monitor with LHC readout electronics ($\beta \approx 100$ m). The BPM electronics is based on a bunch-by-bunch wide-band-time-normaliser principle as described in [12] and is designed to be insensitive to a wide range of temperature and bunch intensity changes. The residual bunch intensity dependence is less than 1% with respect to the BPM half aperture (80 mm). The residual white noise floor of about 2 μm r.m.s for frequencies above 0.1 Hz is visible, indicating the BPM electronics noise.
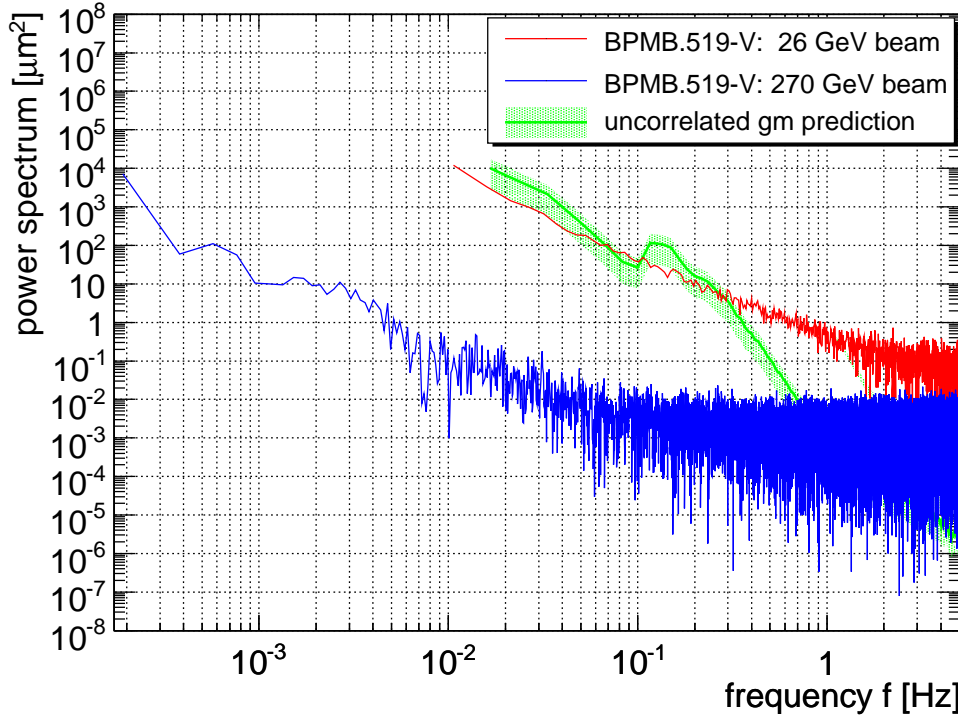

Figure 15: Power spectra of orbit movement at 26 GeV and 270 GeV in the SPS. The white-noise floor of the BPM for high frequencies is visible. The 26 GeV coast might be dominated by slow drifts of the magnetic fields rather than by ground motion. The predicted power spectrum for a worst-case (fully uncorrelated) propagation of the tunnel motion on the beam is shown. In comparison with the actual 270 GeV coasting beam, it is clear that the peak due to the ocean hum is, to a large extent, correlated.

The orbit movements of the 270 GeV beam are much smaller than of the 26 GeV beam, which indicates that the earlier measurements in 2003 may have been dominated by machine-inherent effects such as drifts of magnetic fields rather than by ground motion. A prediction ($\kappa = 40.6 \pm 19.3$) for the spectrum due to uncorrelated tunnel motion is also shown for comparison.

This measurement confirms that in the range of 0.01-0.7 Hz, the tunnel ground motion is highly coherent. The measured quadrupole girder response is about one and does not show damping for this frequency range, which would explain the missing signal. This coherent wave is also visible with a period of about 7 s in the autocorrelation spectra shown in Figure 13. The repetitive pattern further indicates the oscillatory nature of the signal and excludes that the peal

is due to for example slow ramp-like drift or Brownian (random) motion. This measurement is in agreement with seismological measurements performed elsewhere [2, 3, 4]. The measurements described in reference [2, 3] identify and locate the cause of the hum around 0.1 Hz to be due to storms on the northern oceans during the Northern Hemisphere winter and southern oceans during the Southern Hemisphere winter. From the SPS diameter, one can estimate the coherence length of this type and frequency of ground movement to be at least 2 km.

Using the SPS κ amplification factors, the orbit drift can be converted to r.m.s. ground motion drift. In case of the SPS, the white noise floor of the BPMs limits the analysis of orbit drifts to frequencies below 0.1 Hz or drift times above 10 s, respectively. Random ground motion is a statistical process that in first order is described by Brownian motion (see Equation 14).

As described above by Equation 14, the r.m.s. orbit drift, a property of Brownian motion, is proportional to the square root of time. This dependence has been modelled before as an empirical observation by the so called *ATL law* that describes the ground motion variance growth σ^2 as a function of a site-specific drift parameter A_{site}, the time T that is elapsed since the initial condition ($\sigma^2 = 0$), and coherence length L of this type of motion as an additional parameter of this motion [5, 6]:

$$\sigma^2 = A_{\text{site}} \cdot TL \tag{21}$$

However, the direct measurement and fit of the coherence length L is inaccessible using orbits of circular machines due to the filter mechanism of the lattice described above. Using the vertical κ factors for the SPS and fitting a square root dependence on time to the observed orbit drifts (Equation 14), the following SPS ground motion estimate can be obtained:

$$\sigma = A \cdot \frac{1}{\kappa} \sqrt{t} \tag{22}$$

$$A_{\text{vert}}^{\text{SPS}} = 1.2 \cdot 10^{-2} \frac{\mu\text{m}}{\sqrt{\text{s}}} \tag{23}$$

4.3 LEP Orbit Measurements

Over the years, hundreds of thousands of orbits were recorded while LEP was colliding beams for its experiments. The orbit data was analysed to reconstruct the orbit drifts that were compensated by the LEP slow orbit feedback. The data was analysed in the following way, on a fill by fill basis:

- The first orbit recorded with stable colliding beams was used as reference.

- The orbit drift for subsequent orbits was reconstructed by subtracting the orbit from the reference and by deconvoluting any correction of the orbit that took place up to that time with respect to the start of the fill.

- For the horizontal plane, the momentum offset with respect to the nominal momentum was estimated using the dispersion at each monitor. The effect of the estimated momentum offset was subtracted from the orbit. This corrections removes the effect of earth tides and of RF frequency changes that were applied to optimise the luminosity.

- For the vertical plane, the difference orbit was corrected for any contribution due to the eight vertical low-beta quadrupoles ("QS0") using a MICADO correction. This correction

is applied to remove the systematic contribution of the moving quadrupoles that dominated the drifts due to their strength and their abnormal movements. See [13].

- The BPM readings were finally normalised by $\sqrt{\beta}$ before the raw r.m.s drift was evaluated.

This procedure was reproduced for all fills and the data of all fills finally averaged. The data of different years is consistent. In this analysis, the 1999 data, taken at $\approx 100\,\text{GeV}$, is used. Approximately $3 \cdot 10^4$ orbits are used for that year in the average. Figure 16 shows the averaged orbit r.m.s. normalised to the monitor beta function of $100\,\text{m}$, and Figure 17 shows the development in time of the relative spread.
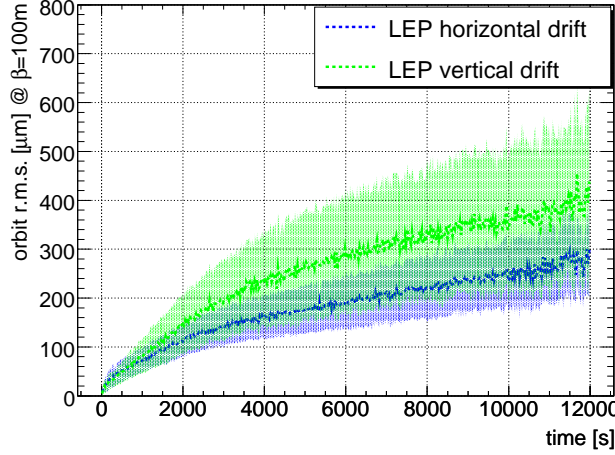

Figure 16: Average vertical and horizontal LEP beam motion drift during operation at $100\,\text{GeV}$. The $\sim \sqrt{t}$ growth with time t is visible.
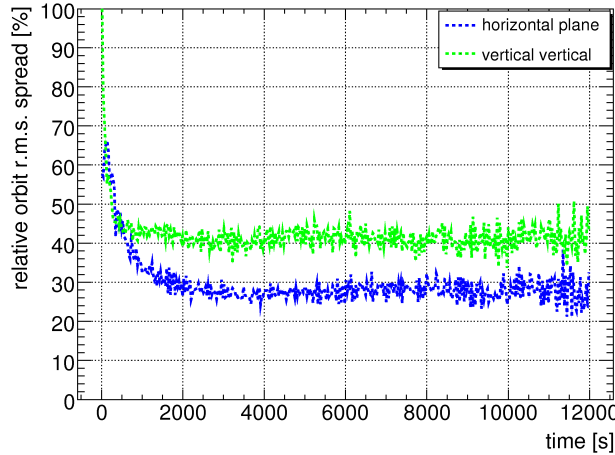

Figure 17: Relative LEP beam motion spread

In the horizontal and vertical plane, the relative spread seems to reach a steady state of about 30% and 40% respectively, after about 2000 seconds, which is about the same spread as expected from the predicted κ value for LEP (Table 3.1). The settling may be due to analysis systematics (correction of QS0 effects and unfolding) and a large number of vertical corrections that were always applied during the first hour of each fill to optimise the luminosity. For

the horizontal plane, the drifts are described well by a $\sqrt{t}$ dependence on time, but for the vertical plane the data follows $\sqrt{t}$ only after $\approx 2000\,\mathrm{s}$. For further analysis, we choose $2000\,\mathrm{s}$ as the minimum time for the analysis of the LEP data.

We assume that the residual beam movement is rather due to the remaining residual ground motion. Using a constant optical amplification factor κ for the SPS and LHC, respectively, one can give an approximation for the average ground motion-induced quadrupole shift as shown in Figure 18.
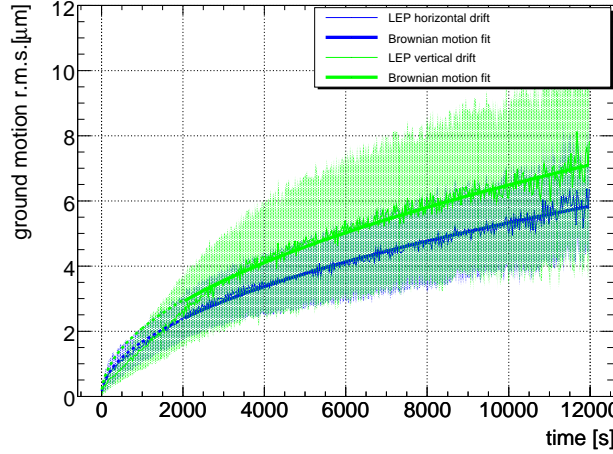

Figure 18: LEP orbit data based ground motion estimate. The $\sqrt{t}$ fit is indicated.

Since the influence of other (unknown) effects cannot be fully excluded, the following estimates should be considered to be an upper limit for ground motion. From LEP $\tilde{\kappa}$ amplification factors the orbit drifts can be converted to r.m.s. ground motion drifts, as seen in Figure 18. A fit to this data to $A \cdot \sqrt{t}$ dependence, an analog to Equation 22 yields the following upper limits for the horizontal and vertical ground motion coefficients:

$$A_{\text{hor}}^{\text{LEP}} \approx 5.3 \cdot 10^{-2} \frac{\mu\mathrm{m}}{\sqrt{\mathrm{s}}} \tag{24}$$

$$A_{\text{vert}}^{\text{LEP}} \approx 6.0 \cdot 10^{-2} \frac{\mu\mathrm{m}}{\sqrt{\mathrm{s}}} \tag{25}$$

The horizontal and vertical parameter spread of about 30 and 40% respectively corresponds and is in good agreement with the prediction for the κ spread shown in Table 2. This may indicates that the remaining drift is due to random ground motion only. We use the LEP values for further analysis, since the LEP data is based on much higher statistics than the SPS (based only on a few cycles).

4.4 Long-term drifts at LEP

It is important to note that the above estimate is only valid for periods up to a month and does not include long-term systematic drift effects such as fault movements and ground water levels. Long-term LEP accelerator alignment studies described in [1] show that the main part of quadrupole movement over several years seems to be linear. The analysis estimates the drift parameter P to be around $5.5\ 10^{-6} \mu\mathrm{m/s}$:

$$\langle \sigma \rangle = 5.5 \cdot 10^{-6} \frac{\mu\mathrm{m}}{\mathrm{s}} \cdot t \tag{26}$$

In the case of systematic linear drifts of the quadrupoles but with individually different drift velocities per quadrupole, the residual orbit would depend only on the initial seed of individual quadrupole drift velocities and would scale linearly with time. On the time scale of a few hours, the systematic contribution is much smaller than the one due to random ground motion. However, due to the different dependence on time, the systematic component largely exceeds the random motion contribution for time scales above a month to years.

In conclusion, in the time scale of a few hours to a month, random ground motion determines the orbit stability, but on large time scales, it is exceeded by the systematic ground motion contribution. For completeness, the beam motion predictions include the random and systematic ground motion drift approximations.

4.5 Estimate for ground motion induced orbit drift at LHC, SPS and in the transfer lines

As an important application, the above ground motion estimates can be used to predict future beam motion at the LHC, the SPS and the transfer lines TI8 and CNGS. Figure 19 and 20 show the predicted LHC orbit movement using the LEP and SPS ground motion estimates and the κ factors for the LHC.
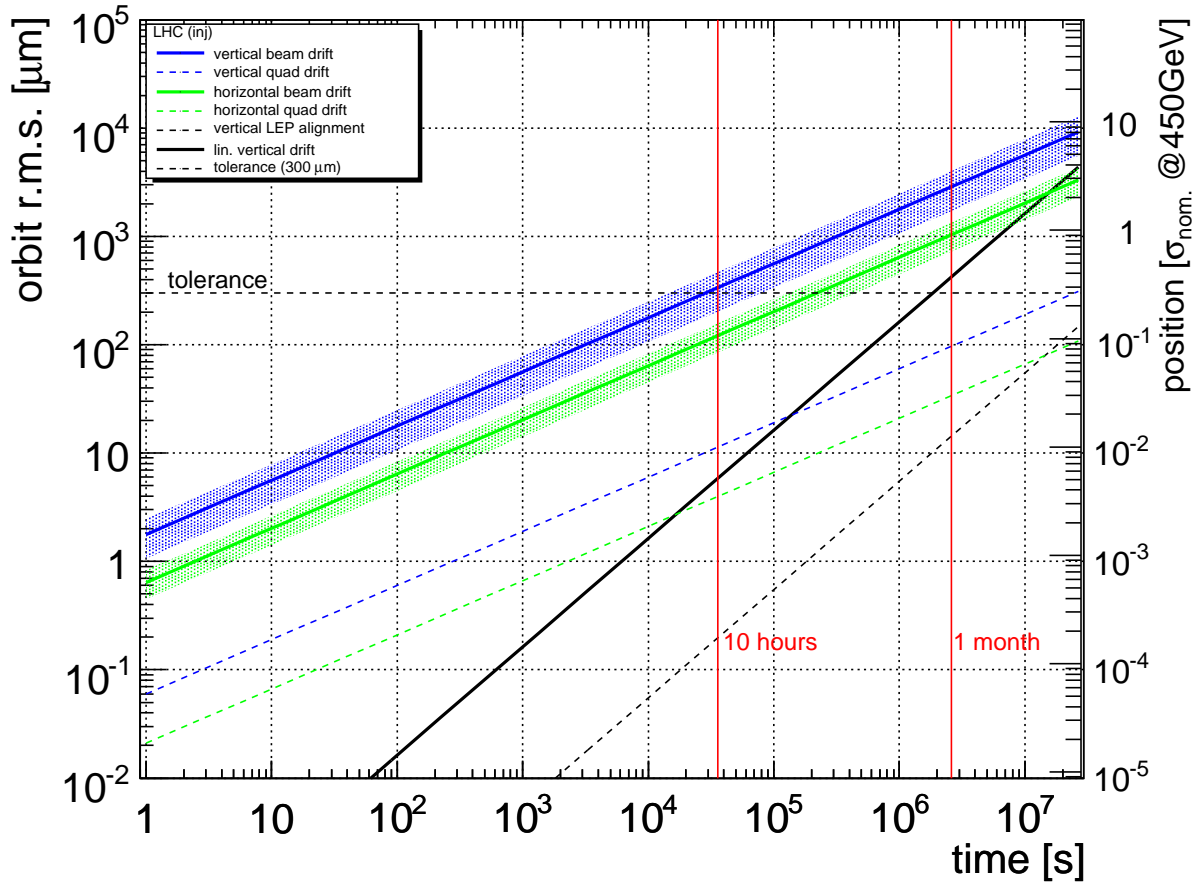

Figure 19: Expected LHC r.m.s. orbit drift due to random ground motion for the injection optics. The drift is given in units of nominal beam size σ (3.75 µm rad emittance and for 450 GeV) on the right scale. The spread corresponds to the spread of parameter κ.

The linear prediction is given for comparison. It is important to note that since the actual beam motion depends on the initial seed of the random quadrupole motion, the spread of the
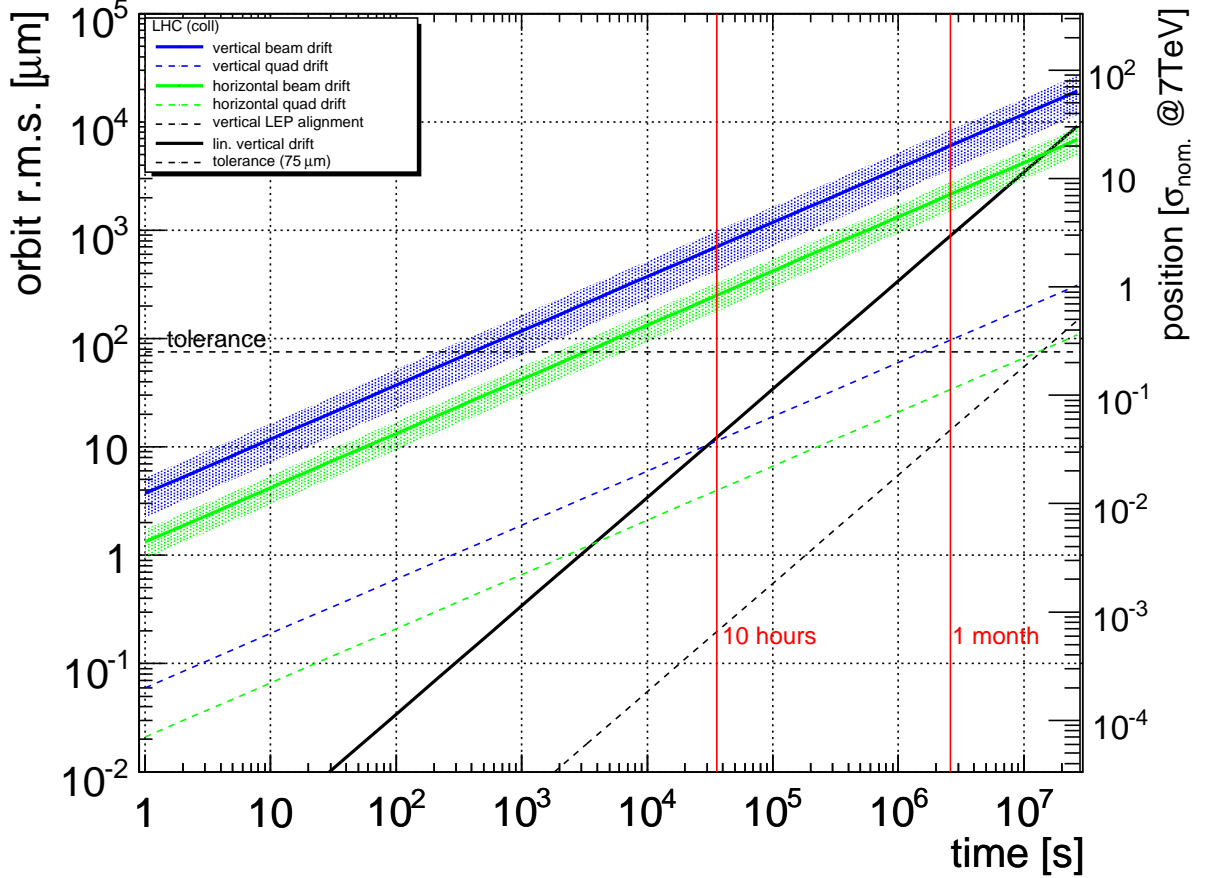
Figure 20: Expected LHC r.m.s. orbit drift due to random ground motion for the collision optics. The drift is given in units of nominal beam size σ (3.75 μm rad emittance and for 7 TeV) on the right scale. The spread corresponds to the spread of parameter κ.

prediction is relatively large ($\approx 30 - 40\%$). Further, the crossing between the random and linear ground motion prediction is visible. The crossing can be used to estimate the time frame where the random ground motion approximation is applicable.

Alignment at the collimator is an important issue during LHC operation. The limit at which the orbit exceeds the required $\approx 0.3\sigma$ (σ: beam size r.m.s.) orbit stability at the collimator jaws is indicated in the plot. It is visible that a critical beam drift due to random ground motion for the LHC injection optics is only reached after about 10 hours. This relaxes the requirement on fast re-steering during injection from the ground motion point of view. However, during injection other effects such as the decay of the persistent currents will dominate orbit drifts.

The stability of the injection is another important parameter for machine operation and protection. Since the injection plateau is only corrected at every injection, one can derive from the estimates that from fill-to-fill the injection orbit will drift in the order of 0.3-0.4 σ due to random ground motion (assuming a fill every about 15 hours).

Similar estimates can be given for the SPS using the corresponding κ factors. The results are shown in Figure 21. After one month, the orbit drift reaches about 1 mm which is of the same magnitude but slightly overestimates the drifts observed during SPS operation (about 500-700 μm per month). Predictions using vertical drift constants obtained with the SPS coasting beam (Equation 23) seem to agree better with operational experiences.
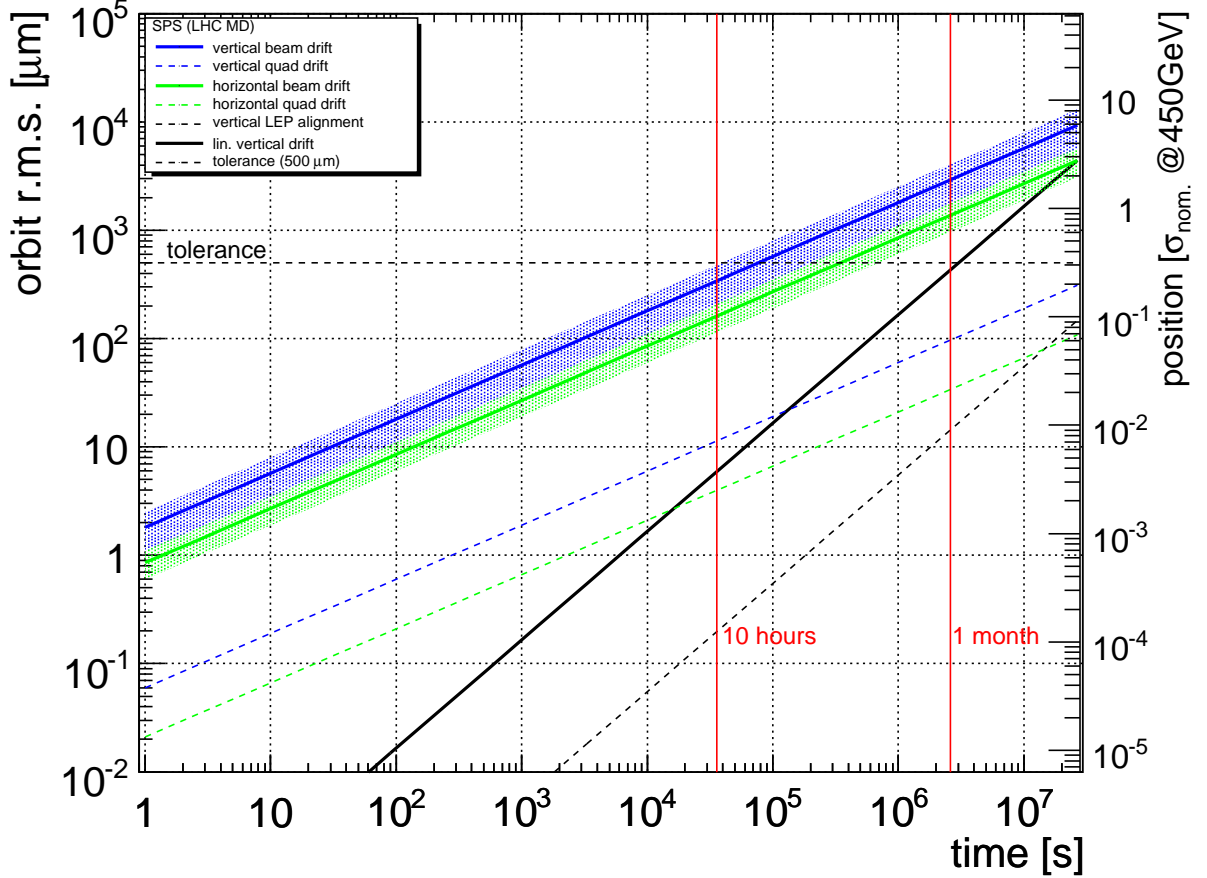
Figure 21: Expected SPS r.m.s. orbit drift due to random ground motion. The corresponding drift in units of nominal beam size σ (3.75 µm rad emittance and for 450 GeV) is given on the right scale. The range corresponds to the parameter κ spread of the model. The tolerance corresponds to the maximum permissible orbit shift at the extraction point to the LHC.

Figure 22 shows the expected drifts in the CNGS and TI8 transfer lines. The computations are done for the location of the CNGS target and the last TI8 beam dump (TED.87765) of the transfer line. In the case of CNGS, the maximum acceptable drift of 500 µm is determined by the target size. Comparing the expected drift at the target over one month with the required stability, it is clear that the drift at the target is dominated rather by the stability of the SPS orbit, the extraction kicker and the septum magnet than by the magnet misalignment due to random ground motion. Similar numbers can be obtained for the TI8 transfer line that was commissioned with beam in 2004. For TI8 the tolerance of about 200 µm corresponds to the largest allowed injection oscillation to ensure good emittance preservation. Measurements described in [16] give an upper limit for the transfer line stability of about $\sigma/8$ and $\sigma/14$, and for a period of about 6 hours and 1 hour respectively. These are compatible with the ground motion prediction. Measurements described in [16] assume that the residual beam jitter is due to the power converter ripple of the transferline magnets, in particular of the extraction septum magnet. The plotted tolerance corresponds to the required upper limit of $\sigma/5$.
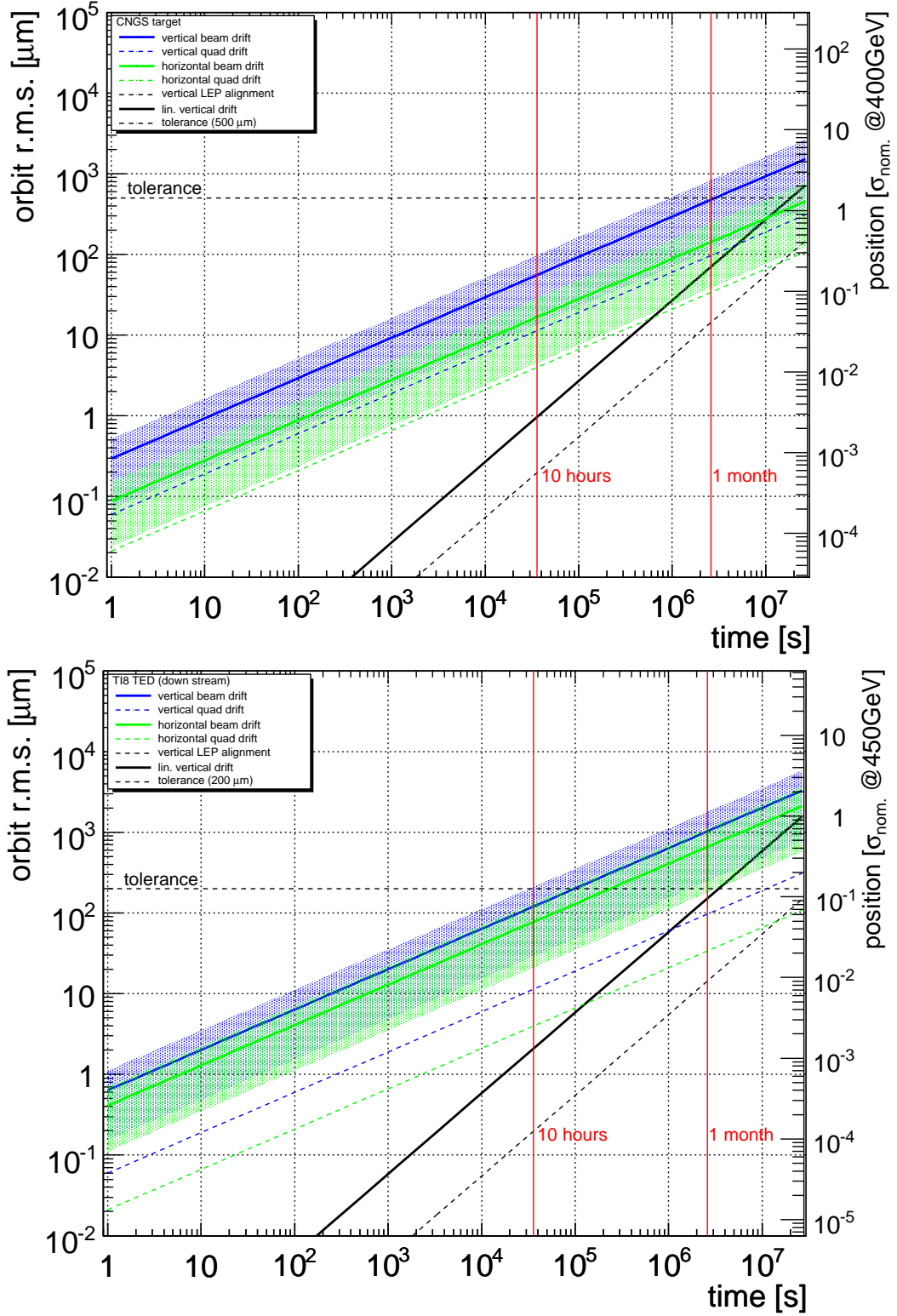
Figure 22: Expected beam drift due to random ground motion at the CNGS Target (top) and TI8 transfer line TED (bottom). The effect of the orbit drift in the SPS at the extraction kicker is not included.

5 Conclusions

The sources of orbit perturbations can be grouped into three groups, machine inherent, machine element failures, and environmental sources. The environmental sources include ground motion, temperature and pressure changes, cultural noise and other effects that are propagated through magnets (mostly quadrupoles) and their girders to the beams. Ground motion affects the beam orbit during all operational phases. The two models that were presented describe the propagation of coherent and random ground motion on the beam orbit both qualitatively and quantitatively.

The ground motion analysis is based on geophone and beam motion measurements in the SPS and LEP. The measured spectra are very quiet and are essentially the same for the SPS and LHC tunnels. The ground motion spectra are barely influenced by so-called 'cultural noise' that originate at the surface.

These measurements confirm that ground motion contribution can be neglected for the LHC for frequencies above 1 Hz, independent of whether the ground motion is correlated or not, assuming that the girder is sufficiently stiff and that its response does not significantly enhance the coherent part of the ground motion spectrum. The actual vibration level of the LHC superconducting magnet, not discussed in this paper, remains to be investigated.

The comparison of beam motion and geophone measurements reveal that the large peak in the ground motion spectrum between 0.01 and 1 Hz is mostly correlated and is of an oscillatory nature. Since the amplification for correlated ground motion on the beam vanishes in that frequency range for SPS, LEP, and LHC, the peak does not measurably influence the beam. In fact, for frequencies below 1 Hz, orbit drifts are dominated by random ground motion.

The drift constants and optical propagation factors (lattice amplification) can be used to predict upper limits for orbit drifts in the LHC, the SPS and the CNGS and TI8 transfer lines. The LHC orbit drift due to random ground motion alone is expected to reach the critical ($0.3\,\sigma$ tolerance for the collimation system only after about 10 hours for the injection optics and after about 0.5 hours for the collision optics under the pessimistic assumption that the orbit feedback is not running. The LHC injection orbit is estimated to drift about $0.3\text{-}0.4\,\sigma$ from fill-to-fill, assuming a fill about every 15 hours. This may slightly reduce the available aperture during the first injection into an empty machine. The drift estimates for the CNGS and TI8 transfer lines are in good agreement with experimental data obtained during the TI8 commissioning and show that, compared to the SPS extraction stability, ground motion-induced orbit drifts in the transfer lines are much smaller than drifts due to the SPS extraction stability.

It is important to note that these predictions only give an upper limit of ground motion-induced orbit drifts. The actual orbit drift may be dominated by the machine environment and operation. The ground motion-induced orbit drift may, over the long-term, be dominated by systematic drifts due to specifics of the LHC tunnel described in [1].

Appendix

Analytic Optical Amplification Approximation

Let ϵ be the r.m.s. quadrupole displacement error. The orbit position shift Δx_i due to a displacement ϵ of the j-th quadrupole with strength k_j and length l_j at the i-th observation point is described by:

$$\Delta x_i = \frac{\sqrt{\beta_i \beta_j} k_j l_j}{2 \sin(\pi Q)} \cdot \cos(\Delta \mu_{ij} - \pi Q) \cdot \epsilon \tag{27}$$

Here $\Delta \mu_{ij}$ is the positive phase advance between the quadrupole and the point of observation. β_j and β_i are the values of the betatron function at the location of the quadrupole and point of observation. Q is the machine tune. The effects of N_q quadrupoles at monitor i add up linearly. If the misalignments are uncorrelated, the variance of the shift is given by,

$$(\Delta x_i)^2 = \sum_j^{N_q} \frac{\beta_i \beta_j (k_j l_j)^2}{(2 \sin(\pi Q))^2} \cos^2(|\Delta \mu_{ij}| - \pi Q) \cdot \epsilon^2 \tag{28}$$

The orbit r.m.s. $(\Delta x)^2$ over N_m monitors (observation points):

$$(\Delta x)^2 = \frac{1}{N_m} \sum_{ij} \frac{\beta_i \beta_j (k_j l_j)^2}{(2 \sin(\pi Q))^2} \cos^2(|\Delta \mu_{ij}| - \pi Q) \cdot \epsilon^2 \tag{29}$$

and considering the frequency dependence $S(f) = \frac{d\epsilon^2}{df}$:

$$\frac{d(\Delta x)^2}{df} = \underbrace{\frac{1}{N_m} \sum_{ij} \frac{\beta_i \beta_j (k_j l_j)^2}{(2 \sin(\pi Q))^2} \cos^2(\Delta \mu_{ij} - \pi Q)}_{\kappa^2(f)} \cdot \frac{d\epsilon^2}{df} \tag{30}$$

$$S_{orbit} = \qquad\qquad\qquad \kappa^2(f) \qquad\qquad\qquad \cdot S_{gm}(f) \tag{31}$$

.

It is possible to perform a rough estimate of κ using the following approximations:

- All quadrupoles have about the same integrated field strengths: $k_j l_j \approx kl = \text{const.}$
- The machine is composed of a regular FODO lattice: focusing quadrupoles have $\beta_{QF} = \text{const.}$ and defocusing quadrupoles have $\beta_{QD} = \text{const.}$ and $\beta_{eff} = \sqrt{\beta_{QF}^2 + \beta_{QD}^2}$.
- Monitors are close to quadrupoles: $\beta_i \approx \beta_{eff}$

leading to the following simplified equation:

$$\kappa^2 = \frac{\beta_{eff}^2 (kl)^2}{(2 \sin(\pi Q))^2} \cdot \frac{1}{N_m} \sum_{ij} \cos^2(\Delta \mu_{ij} - \pi Q) \tag{32}$$

For large machines, the phase advance between monitors and quadrupoles modulo 2π is evenly distributed so that the sum of the $\cos^2$-term over i is approximately to $\frac{1}{2}$. Summing over the number N of FODO cells and taking the square root yields:

$$\kappa = \frac{kl\beta_{eff}}{4\sin(\pi Q)} \cdot \sqrt{N} \qquad (33)$$

Statistical Properties of a Gaussian Process

The movement of a particle with mass m due to a randomly varying force $F(t)$ in a viscous (α being the damping coefficient) medium can be described through STOKE's equation. $F(t)$ shall be symmetric around '0' and is, for instance, GAUSSIAN distributed. For simplicity, without constraining the universality, we assume that the movement is uni-dimensional along the x axis. The differential equation describing the Gaussian process can be written as:

$$m\ddot{x} + \alpha\dot{x} = F(t) \qquad (34)$$

Re-arranging Equation 34 and multiplying with x yields,

$$m\ddot{x} = -\alpha\dot{x} + F(t) \qquad (35)$$

$$mx\ddot{x} = -\alpha x\dot{x} + xF(t) \qquad (36)$$

$$\text{with} \quad x\ddot{x} = \frac{d}{dt}(x\dot{x}) - \dot{x}^2 \qquad (37)$$

$$m \cdot \left[\frac{d}{dt}(x\dot{x}) - \dot{x}^2\right] = -\alpha x\dot{x} + xF(t) \qquad (38)$$

$F(t)$ being a non-regular randomly varying force, it is clear that there cannot be an analytical solution for equation 38. However, it is still possible to derive some statistical properties, such as the mean and root-mean-squared, of the process. Taking the time average $\langle\rangle_t$ leads to:

$$\left\langle m \cdot \left[\frac{d}{dt}(x\dot{x}) - \dot{x}^2\right]\right\rangle_t = \langle -\alpha x\dot{x} + xF(t)\rangle_t \qquad (39)$$

$$m\frac{d}{dt}\langle x\dot{x}\rangle_t - m\langle\dot{x}^2\rangle_t = -\alpha\langle x\dot{x}\rangle_t + \langle xF(t)\rangle_t \qquad (40)$$

The force being randomly distributed, which is equivalent to X and $F(t)$ being fully uncorrelated, the following terms vanish.

$$\langle xF(t)\rangle_t = \langle x\rangle_t\langle F(t)\rangle_t = 0 \qquad (41)$$

One can identify the term describing the average kinetic energy that in kinetic gas-theory is related to the temperature T of the particle through the BOLTZMANN's constant k

$$\frac{1}{2}m\langle\dot{x}^2\rangle_t = \frac{1}{2}kT \qquad (42)$$

resulting in the following equations

$$m\frac{d}{dt}\langle x\dot{x}\rangle_t = kT - \alpha\langle x\dot{x}\rangle_t \tag{43}$$

that can be rearranged to:

$$\left(\frac{d}{dt} + \frac{\alpha}{m}\right)\langle x\dot{x}\rangle_t = \frac{kT}{\alpha} \tag{44}$$

The following ansatz can be used to solve the differential equation 44:

$$\langle x\dot{x}\rangle_t = C \cdot e^{-\frac{\alpha}{m}t} + \frac{kT}{\alpha} \tag{45}$$

with C being a constant that has to be adjusted in order to satisfy the initial conditions

$$\langle x\dot{x}\rangle_{t=0} := 0 \leftrightarrow 0 = C + \frac{kT}{\alpha} \tag{46}$$

using the relation

$$\langle x\dot{x}\rangle_t = \frac{1}{2}\frac{d}{dt}\langle x^2\rangle_t \tag{47}$$

that leads to:

$$\frac{1}{2}\frac{d}{dt}\langle x^2\rangle_t = \frac{kT}{\alpha}\left(1 - e^{-\frac{\alpha}{m}t}\right) \tag{48}$$

After integration, one gets the following important relation for $\langle x^2\rangle_t$:

$$\langle x^2\rangle_t = \frac{2kT}{\alpha}\left[t - \frac{m}{\alpha}\left(1 - e^{-\frac{\alpha}{m}t}\right)\right] \tag{49}$$

One can easily see, after applying the time average on Equation 34 directly, that the mean $\mu = \langle x\rangle_t$ exponentially vanishes for timescales:

$$\boxed{\lim_{t\to\infty}\mu \sim \lim_{t\to\infty} e^{-\frac{\alpha}{m}t} = 0} \tag{50}$$

The root-mean-squared of the process is defined as:

$$\sigma_{rms}^2 = \langle x^2 - \mu^2\rangle_t = \langle x^2\rangle_t - \langle x\rangle_t^2 \tag{51}$$

since the mean μ vanishes for Gaussian processes:

$$\sigma_{rms} = \sqrt{\langle x^2\rangle_t} \tag{52}$$

Expanding the exponential dependence of Equation 49, one can derive the following two solutions for the r.m.s. depending on the parameter $\frac{m}{\alpha}$:

1. for $t \gg \frac{m}{\alpha}$ (small timescales)

$$\sigma_{rms} = \sqrt{\frac{kT}{m}} \cdot t \tag{53}$$

2. for $t \ll \frac{m}{\alpha}$ (large timescales)

$$\boxed{\sigma_{rms} = \sqrt{\frac{2kT}{\alpha}} \cdot \sqrt{t}} \tag{54}$$

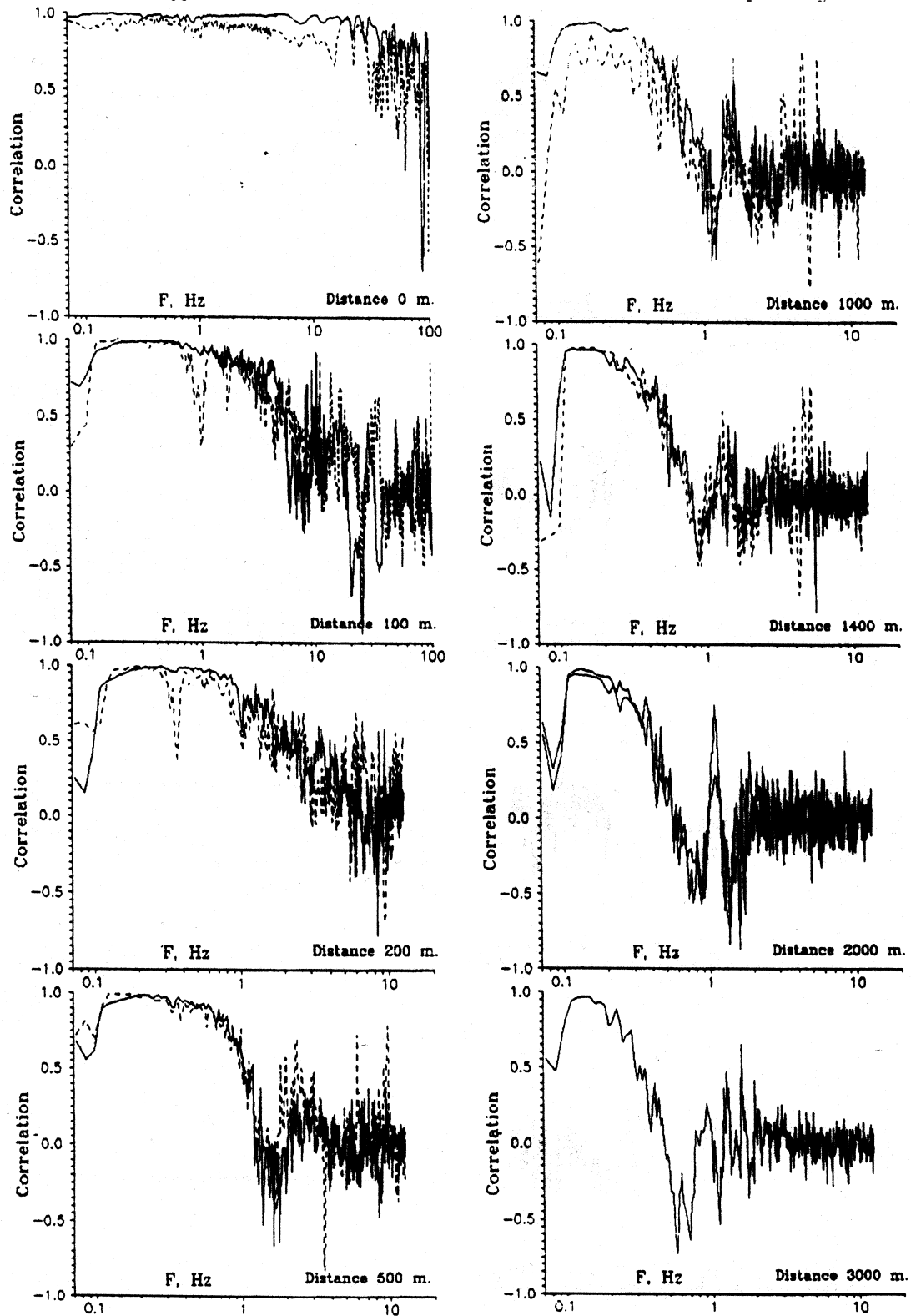# Correlation Length in the LEP Tunnel as a Function of Frequency - REPRINT

Figure 23: Correlation between two horizontal probes oriented transverse to the LEP tunnel. Probes are 0 m, 100 m, 200 m, 500 m, 1000 m, 1400 m, 2000 m and 3000 m apart. Reprint of reference [10]. It is visible that the correlation decreases with the probe distance.
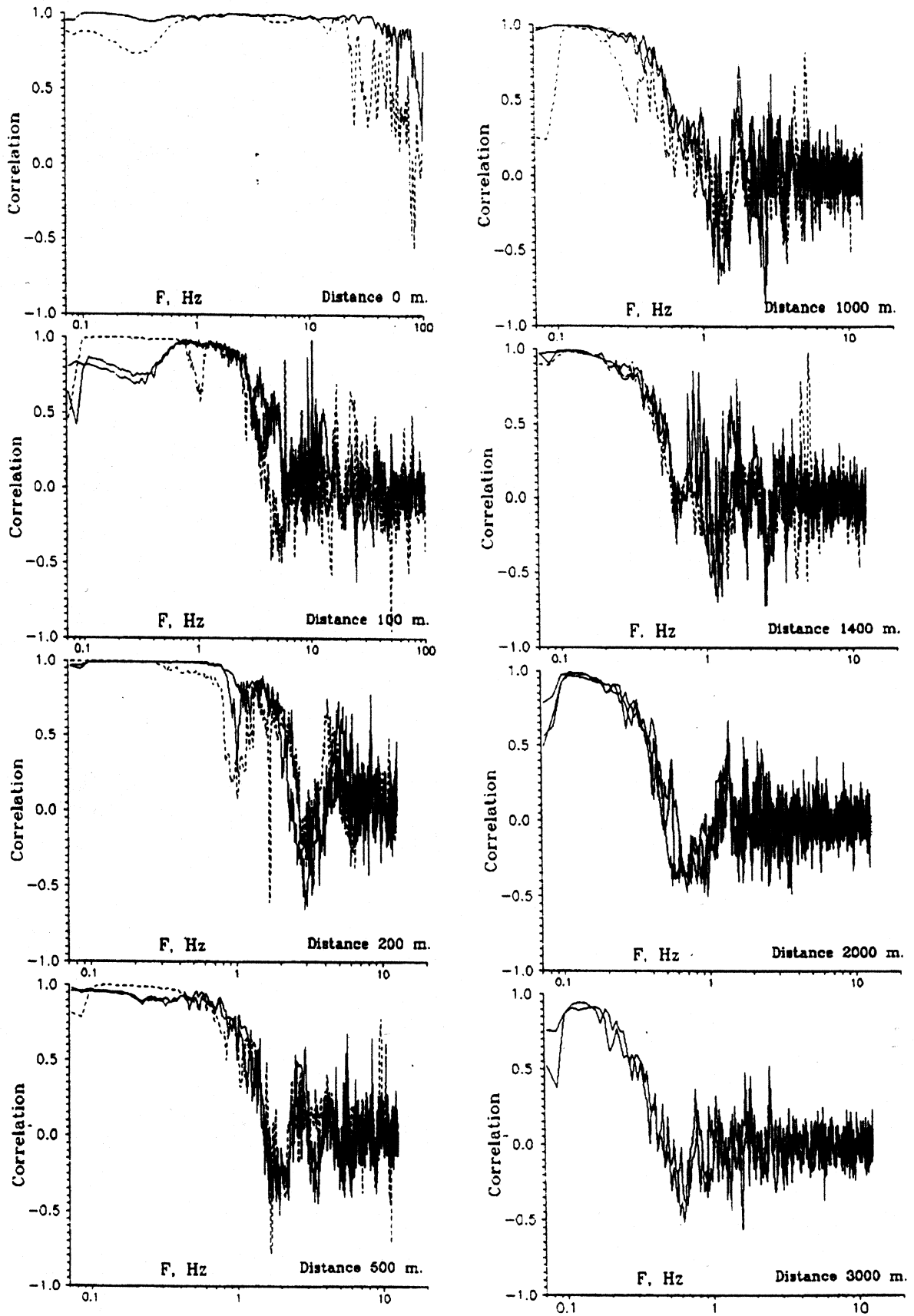
Figure 24: Correlation between two vertical probes oriented transverse to the LEP tunnel. Probes are 0 m, 100 m, 200 m, 500 m, 1000 m, 1400 m, 2000 m and 3000 m apart. Reprint of [10]. It is visible that the correlation decreases with the probe distance.

References

[1] R. Pitthan, "LEP Vertical Tunnel Movements - Lessons for Future Colliders", CERN CLIC-Note 422, LCC-0028 and SLAC-PUB-8286, CERN, Geneva, 1999

[2] F. Marillier, U. Eichenberger and A. Sommaruga, "Seismic Synthesis of the Swiss Molasse Basin", Institute de Géophysique - UNI Lausanne, Lausanne, 2004

[3] G. Amberger, "La Molasse du Bassin Genevois", published in: "Cahiers de la Faculté des Science", UNI Geneva, Geneva, 1987

[4] Shigeru Takeda Hiroshi Matsumoto Masakazu Yashioka and Yasunori Takeuchi, "Incoherent Ground Motion", Proceedings of EPAC 2000, Vienna, Austria, pp. 2394, 2000

[5] V. Shiltsev, "Space-Time Ground Diffusion: The ATL Law for Accelerators", DESY-MEA-95-02, 1995

[6] A. Wolski and N.J. Walker, "A Model of ATL Ground Motion For Storage Rings", Proceedings of the PAC Conference, Portland,USA, 2003

[7] J. Rhie and B. Romanowicz, "Excitation of Earth's Continuous Free Oscillations by Atmosphere-Ocean-Seafloor Coupling", Nature, vol. 431, p. 552-556, September 2004

[8] A. Friedrich et al., "Ocean-generated Microseismic Noise located with the Gräfenberg Array", Journal of Seismology 2, p. 47-64, 1998

[9] V.E. Balakin et al., "Measurements of Seismic Vibrations in the CERN TT2A Tunnel for Linear Collider Studies", CERN-SL/93-30 and CLIC-Note 191, CERN, Geneva, 1993

[10] V.M. Juravlev et al., "Investigations of Power and Spatial Correlation Characteristics of Seismic Vibrations in the CERN LEP Tunnel for Linear Collider Studies", CERN-SL/93-53 and CLIC-Note 217, CERN, Geneva, 1993

[11] Matteo Frigo and Steven G. Johnson, "FFTW - The Fastest Fourier Transform in the West", Massachusetts Institute of Technology, 1999, *http://www.fftw.org/*

[12] Daniel Cocq, "The Wide Band Normaliser - A New Circuit to Measure Transverse Bunch Position in Accelerators and Colliders", NIMA 416, Elsevier, 1998

[13] F. Tecker, "Closed Orbit Feedback from Low-Beta Quadrupole Movements at LEP", CERN SL-97-026, 1997

[14] Eberhard Keil, "Effect of Plane Ground Waves on the Closed Orbit in Circular Machines", CERN SL/97-61 (AP), 1997

[15] L. Vos, "Ground Motion Model for the LHC", LHC Project Report 444, 2000

[16] J. Wenninger, B. Goddard, V. Kain, J. Uythoven, "Beam Stability of the LHC Beam Transfer Line TI 8", LHC Project Report 821 and Proceedings of PAC05, Knoxville/TN,USA, 2005